AWARD ACCOUNTS
SPSJ Award Accounts
Slow Dynamics in Homopolymer Liquids

By Hiroshi WATANABE[*]

Dynamic physical properties of homopolymer liquids relax through global motion of the polymer chains over their dimension. This motion is affected by a variety of factors. For high molecular weight (M) chains, the entanglement retards the global motion to affect the properties. This entanglement effect changes with the chain architecture as well as the molecular weight distribution. The effect of the chain architecture on the global chain dynamics is found also for non-entangled low-M chains as well. This article gives a very brief summary of the experimental facts and molecular interpretations for these effects.

KEY WORDS: Homopolymer Liquid / Relaxation / Slow Dynamics / Entanglement / Viscoelastic Property / Dielectric Property / Type-A Dipole /

Needless to say, *flexible polymer chains* are composed of monomeric units covalently connected in a thread-like structure. In a local length scale, they have their own chemical functionalities such as the polorizability and electron susceptibility to exhibit intrinsic spectroscopic properties, for example, optical and electronic properties. In this sense, chemically different polymers cannot be regarded as the same class of materials. At the same time, however, the threadlike structure of polymer chains allows such chemically different chains to exhibit some universal properties. For example, flexible linear polymer melts exhibit the universal power law dependence of the zero-shear viscosity η_0 on the molecular weight M, $\eta_0 \propto M^\alpha$ with $\alpha \cong 1$ and $\cong 3.5$ in low- and high-M regimes, respectively.[1] This dependence and related slow viscoelastic relaxation of polymer melts are believed to result from the fundamental thread-like structure of polymer chains irrespective of their chemical details. *Scientifically*, it is very interesting to explore a relationship(s) between such universal behavior of flexible polymer chains and their slow dynamics and further examine the factors that affect the slow dynamics and properties.

This article follows the above viewpoint to give a very brief review of slow viscoelastic and dielectric relaxation behavior of homopolymer liquids. We place our main focus on homopolymer systems where the entanglement resulting from mutual uncrossability of real polymer chains plays the essential role. The entanglement, often modeled as mutual winding/hooking of threads, is equivalent to a topological constraint for thermal motion of the polymer chains that changes its magnitude according to the time and length scales. The linear and nonlinear viscoelastic behavior and related dielectric behavior of homopolymer melts/solutions are summarized on the basis of this molecular understanding.
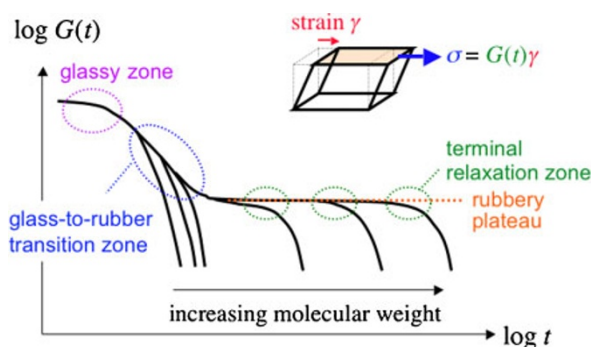

Figure 1. A schematic illustration of viscoelastic relaxation modulus of flexible linear polymers.

BASICS

Molecular Expression of Viscoelastic Relaxation Function

For a series of chemically identical linear polymer melts having different molecular weights M, Figure 1 schematically shows the relaxation behavior of shear stress $\sigma(t)$ under a small step shear strain γ:[1] The relaxation modulus, $G(t) \equiv \sigma(t)/\gamma$, is double-logarithmically plotted against the time t after imposition of strain. The decay of $G(t)$ undoubtedly results from thermal motion of the polymer chains.

As shown in Figure 1, the glassy zone at short t is followed by the glass-to-rubber transition zone and further by the terminal relaxation (or flow) zone at long t. For polymers having small M, the glass-to-rubber transition zone is smoothly connected to the terminal relaxation zone, and their viscoelastic terminal relaxation time $\langle\tau_G\rangle$ (defined later by eq 9) scales with M as $\langle\tau_G\rangle \propto M^\alpha$ with $\alpha \cong 2$. In contrast, for linear polymers with M larger than a critical molecular weight M_c, the terminal relaxation does not occur immediately after comple-

Institute for Chemical Research, Kyoto University, Uji, Kyoto 611-0011, Japan
[*]To whom correspondence should be addressed (Tel: +81-774-38-3135, Fax: +81-774-38-3139, E-mail: hiroshi@scl.kyoto-u.ac.jp).

tion of the glass-to-rubber transition, and $G(t)$ exhibits a rubber-like plateau before the terminal relaxation occurs. The viscoelastic $\langle \tau_G \rangle$ of these high-M polymers scales as $\langle \tau_G \rangle \propto M^\alpha$ with $\alpha \cong 3.5$. This $\langle \tau_G \rangle$ is larger, in magnitude, than that extrapolated from the $\langle \tau_G \rangle$-M relationship for the low-M polymers, meaning that the motion of high-M polymer chains (reflected in the relaxation of $G(t)$) is retarded compared to that extrapolated from the behavior of low-M chains. This retardation is attributed to some topological constraint, referred to as the *entanglement*, for the large-scale motion of high-M polymers.

The molecular understanding of the stress relaxation requires us to relate $\sigma(t)$ to the conformational variable of the chains. Obviously, the length scale of the thermal motion of the chain changes with a time scale of our focus. In short time scales, only the local motion (often referred to as the segmental motion) can be activated and the chain conformation over a larger length scale is frozen. In this time scale, the monomeric segment behaves more or less as a flat slab as schematically shown in Figure 2, because the torsional motion around the chemical bonds in the chain backbone has not been fully activated. The chain cannot be regarded as a continuous thread in such short time scales. On the other hand, in long time scales where this torsional motion occurs actively to equilibrate successive monomeric segments, the chain can be regarded as a thread composed of larger (coarse-grained) flexible segments referred to as *subchains*; *cf.* Figure 2. Thus, the molecular expression of the stress $\sigma(t)$ changes with the time scale, as demonstrated in extensive rheo-optical studies by Inoue, Osaki, and coworkers:[2–6] They found that the stress relaxing in short time scales is related to the planer orientational anisotropy of the slab-like monomeric segments (the anisotropy of the normal vector δ shown in Figure 2) as well as to distortion of their packing state under the strain, while the stress relaxing in long time scales is related to axial orientational anisotropy of those segments and subchains (the anisotropy of the bond vectors $\mathbf{b}$ and $\mathbf{u}$).

Thus, for the slow (terminal) viscoelastic relaxation of homopolymer liquids focused in this article, we may assume the Gaussian statistics for the subchains and express the stress tensor $\sigma(t)$ in terms of conformational variable of the subchains. For monodisperse chains each composed of N subchains (either linear or branched chains), this expression reads[7–10]

$$\sigma(t) = 3\nu N k_B T \left\{ \frac{1}{N} \sum_{n=1}^{N} \left\langle \frac{\mathbf{u}(n,t)\mathbf{u}(n,t)}{gb^2} \right\rangle \right\} - p\mathbf{I} \qquad (1)$$

where k_B is the Boltzmann constant, T is the absolute temperature, ν is the number density of the chains, g is the number of the monomeric segments of step length b per subchain, p is the isotropic pressure, and $\mathbf{I}$ is the unit tensor. (For polydisperse chains, the stress tensor is given as a sum of $\sigma(t)$ specified by eq 1). In eq 1, $\mathbf{u}(n,t)$ is the bond vector (end-to-end vector) of n-th subchain of the chain at time t (*cf.* Figure 2), $\mathbf{uu}$ is the dyadic of $\mathbf{u}$, and $\langle \cdots \rangle$ indicates the ensemble average over the chains in the system. Note that the
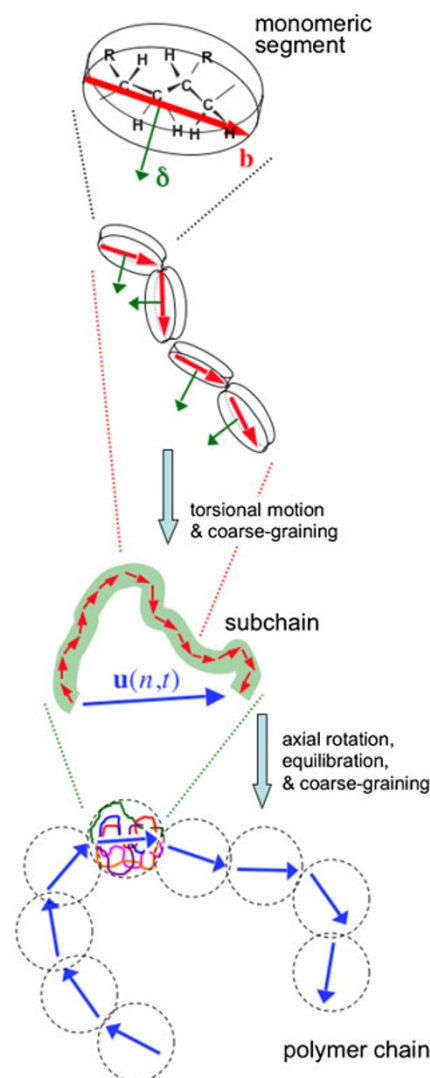

Figure 2. A schematic illustration of hierarchical structure of flexible linear polymers.

$(1/N)\Sigma_{n=1}^{N} \langle \mathbf{uu}/gb^2 \rangle$ term in eq 1 represents the axial orientational anisotropy of a subchain averaged for all subchains in the system and the stress is essentially given as a product of this average and the total number of subchains, νN. Eq 1 is equivalent to the stress-optical rule[2–7] established in long time scales (rubbery plateau and terminal relaxation zones shown in Figure 1).

The shear stress $\sigma(t)$ is given as the shear component of $\sigma(t)$. Specifically, the linear viscoelastic relaxation modulus $G(t)$ under a small step shear strain γ can be conveniently expressed as[7–10]

$$G(t) = \frac{3\nu k_B T}{\gamma} \sum_{n=1}^{N} S(n,t) \quad \text{with}$$

$$S(n,t) = \frac{1}{a^2} \langle u_x(n,t) u_y(n,t) \rangle \qquad (2)$$

where the shear and shear gradient directions have been chosen as the x and y directions and all subchains are considered to
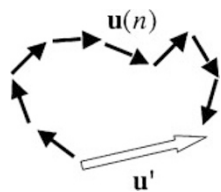
Figure 3. A schematic illustration of bond vectors **u** of subchains and **u′** of a coarse-grained subchain.

have the same average size, $a = \langle gb^2 \rangle^{1/2}$. The shear orientation function $S(n,t)$ represents the average anisotropy of n-th subchain. In the linear viscoelastic regime, the chain dynamics is negligibly affected by the strain and thus the relaxation of $S(n,t)$ reflects the equilibrium motion of the chains. Since flexible chains have a huge freedom of their intra-chain motion, $G(t)$ of these chains exhibits a relaxation mode distribution and is phenomenologically expressed as

$$G(t) = G(0)\mu(t) \quad \text{with} \quad \mu(t) = \sum_{p \geq 1} h_{p;G} \exp\left(-\frac{t}{\tau_{p;G}}\right) \quad (3)$$

where $\tau_{p;G}$ and $h_{p;G}$, respectively, represent the characteristic time and normalized intensity of p-th viscoelastic relaxation mode of the normalized viscoelastic relaxation function, $\mu(t) \equiv G(t)/G(0)$ with $G(0)$ being the initial modulus. The relaxation mode is indexed in the decreasing order of $\tau_{p;G}$ (*i.e.*, $\tau_{1;G} > \tau_{2;G} > \tau_{3;G} > \cdots$).

Here, a comment needs to be made for a choice of the subchain utilized in eqs 1 and 2. At first sight, the stress value may appear to change with this choice. However, this is not the case, as can be noted from a simple example explained below.[9] We consider successive β subchains having the end-to-end vectors $\mathbf{u}(n)$ ($n = 1, 2, \cdots, \beta$). These subchains are *mutually equilibrated* while their total end-to-end vector $\mathbf{u}' = \Sigma_{n=1}^{\beta} \mathbf{u}(n)$ is kept constant; *cf.* Figure 3. Then, $\mathbf{u}(n)$ can be expressed as $\mathbf{u}(n) = \mathbf{u}'/\beta + \mathbf{v}(n)$, where $\mathbf{v}(n)$ is an isotropically distributed vectors being uncorrelated to $\mathbf{u}'$ ($\langle \mathbf{u}'\mathbf{v}(n)\rangle = \mathbf{0}$) and satisfying $\Sigma_{n=1}^{\beta} \mathbf{v}(n) = \mathbf{0}$, and the stress sustained by the β subchains is given by (*cf.* eq 1)

$$\boldsymbol{\sigma} = 3k_B T \sum_{n=1}^{\beta} \left\langle \frac{\mathbf{u}(n)\mathbf{u}(n)}{gb^2} \right\rangle + \text{isotropic term}$$

$$= 3k_B T \left\langle \frac{\mathbf{u}'\mathbf{u}'}{\beta gb^2} \right\rangle + \text{isotropic term} \quad (4)$$

Namely, the deviatoric part of the sum of the $\langle \mathbf{u}\mathbf{u}/gb^2 \rangle$ terms for the β subchains coincides with that of the $\langle \mathbf{u}'\mathbf{u}'/\beta gb^2 \rangle$ term defined for a larger, more coarse-grained subchain containing βg monomeric segments. This coincidence indicates that the subchains utilized in the stress expression can be arbitrarily chosen *given that the monomeric segments in each subchain are mutually equilibrated.*[9] (This equilibration guarantees $\langle \mathbf{u}'\mathbf{v}(n)\rangle = \mathbf{0}$ to give the above coincidence.) In other words, an internally non-equilibrated subchain cannot be utilized as the stress-sustaining unit in eq 1. This fact becomes essential in our later discussion of a molecular picture for entangled chains referred to as *dynamic tube dilation*.

Molecular Expression of Dielectric Relaxation Function

Now, we turn our attention to the dielectric behavior of polymers *at equilibrium* (under no strain/flow). The experimentally observed dielectric relaxation is defined with respect to the macroscopic polarization induced under an electric field. In a microscopic view, this relaxation detects fluctuation of the microscopic polarization $\mathbf{p}(t)$ given by a sum of molecular dipoles in the long time scale of our interest, and the normalized dielectric relaxation function $\Phi(t)$ coincides with the auto-correlation function of $\mathbf{p}$, $\Phi(t) = \langle \mathbf{p}(t) \cdot \mathbf{p}(0)\rangle / \langle \mathbf{p}^2 \rangle$.[11]

Most of polymers have so-called type-B dipoles attached to the monomeric segments in the direction perpendicular to the chain backbone, and fluctuation of these dipoles leads to the fast dielectric relaxation often referred to as the segmental relaxation.[12,13] However, some polymers such as *cis*-polyisoprene (PI) also have so-called type-A dipoles parallel along the chain backbone.[12,13] These chains are hereafter referred to as type-A chains. For linear monodisperse chains having no inversion of the type-A dipoles along the chain backbone, the sum of these dipoles per chain is proportional to the end-to-end vector $\mathbf{R}$ and thus the terminal dielectric relaxation detects the global (large-scale) motion of the chain over a length scale of $\mathbf{R}$. The global motion is dielectrically detected also for a chain having once-inverted type-A dipoles. (An illustration of this dipole-inverted chain is shown later in Figure 9.) Thus, in the long time scale of our interest, $\Phi(t)$ defined for these linear chains can be conveniently expressed as[13]

$$\Phi(t) = \frac{1}{N} \sum_{n=1}^{N} \sum_{m=1}^{N} \xi(n)\xi(m) C(n,t;m) \quad \text{with}$$

$$C(n,t;m) = \frac{1}{a^2} \langle \mathbf{u}(n,t) \cdot \mathbf{u}(m,0)\rangle \quad (5)$$

Here, $C(n,t;m)$ is a *local correlation function* that represents orientational correlation of the bond vectors $\mathbf{u}(n,t)$ and $\mathbf{u}(m,0)$ of n-th and m-th subchains at two separate times, t and 0: $C(n,t;m)$ satisfies an initial condition $C(n,0;m) = \delta_{nm}$ because of the Gaussian feature of the chain. The index $\xi(n)$ appearing in eq 5 has a value of 1 and -1 for the cases that the sum of the monomeric type-A dipoles in n-th subchain is parallel and anti-parallel to $\mathbf{u}(n,t)$, respectively. Specifically, for a linear chain having non-inverted type-A dipoles, $\xi(n) = 1$ for $n = 1 - N$ and eq 5 reduces to a familiar expression, $\Phi(t) = \langle \mathbf{R}(t) \cdot \mathbf{R}(0)\rangle / \langle R^2 \rangle$.[13] (Note that $\Sigma_{n=1}^{N} \mathbf{u}(n,t) = \mathbf{R}(t)$.) Eq 5 is valid also for branched chains given that the sum is taken over all subchains in all portions (branches/trunks) of the chain and N is regarded as a total number of subchains per chain. For the linear as well as branched chains, $\Phi(t)$ exhibits a relaxation mode distribution reflecting the freedom of the intra-chain motion and is phenomenologically expressed as

$$\Phi(t) = \sum_{p \geq 1} h_{p;\varepsilon} \exp\left(-\frac{t}{\tau_{p;\varepsilon}}\right) \quad \text{with} \quad \tau_{1;\varepsilon} > \tau_{2;\varepsilon} > \tau_{3;\varepsilon} > \cdots \quad (6)$$

where $\tau_{p;\varepsilon}$ and $h_{p;\varepsilon}$, respectively, represent the characteristic time and normalized intensity of p-th dielectric relaxation mode.

As can be easily noted from eq 5, the global motion of type-A chains results in full relaxation of $\Phi(t)$. Thus, the dielectric $\Phi(t)$ and the linear viscoelastic $G(t)$ of these chains reflect the same global motion. However, we should also note an important difference: $\Phi(t)$ is related to the first moment average of the subchain bond vector $\mathbf{u}(n, t)$ *at time t* (*cf.* eq 5), while $G(t)$ is equivalent to the second moment average of $\mathbf{u}(n, t)$ (*cf.* eq 2). Thus, there is no unique relationship between the functional forms of $\Phi(t)$ and $G(t)$.[9,13] For example, the relaxation mode distribution of $\Phi(t)$ of the linear type-A chain is exactly the same for the Rouse and reptation mechanisms but the mode distribution of $G(t)$ is quite different for these mechanisms.[9] This lack of unique relationship in turn enables us to compare the dielectric and viscoelastic quantities of type-A chains to experimentally examine details of the chain dynamics, as explained later for a test of the molecular picture of dynamic tube dilation and for an analysis of motional coherence along the chain backbone.

SLOW DYNAMICS AT EQUILIBRIUM: A COARSE-GRAINED VIEW

Overview of Linear Viscoelastic/Dielectric Behavior of Entangled Type-A Chains

For a representative type-A polymer, high-*cis* polyisoprene (PI), viscoelastic and dielectric behavior has been examined extensively.[9,12–47] PI has just small dipole moments and thus the dipole-dipole interaction negligibly affects the chain dynamics. In addition, PI chains of various architectures can be easily synthesized anionically. For these reasons, PI has been serving as a very good model material for the study of slow dynamics.

As an example of the dynamic behavior of PI, Figure 4 shows angular frequency (ω) dependence of the linear viscoelastic storage and loss moduli, G' and G'', a decrease of the dynamic dielectric constant, $\varepsilon_0 - \varepsilon'(\omega)$ with ε_0 = static dielectric constant, and the dielectric loss, $\varepsilon''(\omega)$, for three PI samples of different architectures, linear PI[40] with the molecular weight $M = 308 \times 10^3$ (top panel), 6-arm star-branched PI[38] with the arm molecular weight $M_{arm} = 59.0 \times 10^3$ (middle panel), and Cayley-tree PI[45] with the inner and outer arm molecular weights $M_{in} = 24.7 \times 10^3$ and $M_{out} = 12.3 \times 10^3$ (bottom panel). The Cayley-tree PI has the tri-functionally branched inner arms each having two outer arms (see the illustration in the bottom panel). The molecular weights of the chains/arms are larger than the entanglement molecular weight, $M_e = 5 \times 10^3$ for bulk PI,[1] and their relaxation is significantly affected by the entanglement. The linear PI sample have non-inverted type-A dipoles and its dielectric relaxation detects the auto-correlation of the end-to-end vector $\mathbf{R}$, *i.e.*, $\Phi(t) = \langle \mathbf{R}(t) \cdot \mathbf{R}(0) \rangle / \langle R^2 \rangle$; *cf.* eq 5 with $\xi(n) = 1$ for $n = 1 - N$. The star PI has the dipoles diverging from the central branching point and its dielectric relaxation detects the auto-correlation of the end-to-end vector of the arm.[38] The Cayley-tree PI also has the diverging dipoles and its dielectric relaxation detects the auto-correlation of a sum of the end-to-end vectors of the inner and outer arms.[45]
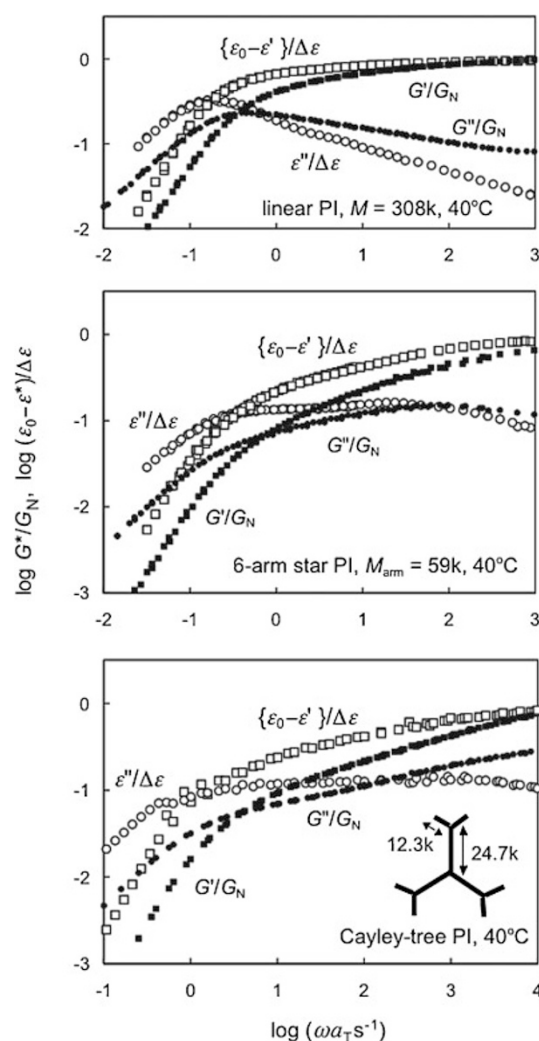

Figure 4. Angular frequency (ω) dependence of the linear viscoelastic storage and loss moduli, G' and G'', a decrease of the dynamic dielectric constant, $\varepsilon_0 - \varepsilon'(\omega)$ with ε_0 = static dielectric constant, and the dielectric loss, $\varepsilon''(\omega)$, obtained at 40 °C for linear PI[40] with $M = 308 \times 10^3$ (top panel), 6-arm star-branched PI[38] with $M_{arm} = 59.0 \times 10^3$ (middle panel), and Cayley-tree PI[45] with $M_{in} = 24.7 \times 10^3$ and $M_{out} = 12.3 \times 10^3$ (bottom panel). The data are normalized by respective relaxation intensities. The data taken from refs 38, 40, and 45 with permission.

The time-temperature superposition held for the viscoelastic and dielectric data of those PI samples measured at various temperatures T, and the shift factor a_T was the same for those data.[38,40,45] In Figure 4, these data are normalized by the viscoelastic and dielectric relaxation intensities, G_N (= entanglement plateau modulus) and $\Delta\varepsilon$, and plotted against a reduced frequency ωa_T at a reference temperature, $T_r = 40$ °C. Note that G_N is equivalent to the initial modulus for the slow viscoelastic relaxation, $G(0)$ appearing in eq 3.

The normalized G'/G_N (filled squares in Figure 4), G''/G_N (filled circles), $\{\varepsilon_0 - \varepsilon'\}/\Delta\varepsilon$ (unfilled squares), and $\varepsilon''/\Delta\varepsilon$ data (unfilled circle) are related to the normalized viscoelastic and dielectric relaxation functions, $\mu(t)$ and $\Phi(t)$, through the Fourier transformation and are expressed in terms of the

viscoelastic and dielectric relaxation spectra $\{h_{p;G}, \tau_{p;G}\}$ and $\{h_{p;\varepsilon}, \tau_{p;\varepsilon}\}$ as[1,9] (*cf.* eqs 3 and 6)

$$G'(\omega)/G_N = \sum_{p\geq 1} h_{p;G} \frac{\omega^2 \tau_{p;G}^2}{1 + \omega^2 \tau_{p;G}^2},$$

$$G''(\omega)/G_N = \sum_{p\geq 1} h_{p;G} \frac{\omega \tau_{p;G}}{1 + \omega^2 \tau_{p;G}^2} \qquad (7)$$

$$\{\varepsilon_0 - \varepsilon'(\omega)\}/\Delta\varepsilon = \sum_{p\geq 1} h_{p;\varepsilon} \frac{\omega^2 \tau_{p;\varepsilon}^2}{1 + \omega^2 \tau_{p;\varepsilon}^2},$$

$$\varepsilon''(\omega)/\Delta\varepsilon = \sum_{p\geq 1} h_{p;\varepsilon} \frac{\omega \tau_{p;\varepsilon}}{1 + \omega^2 \tau_{p;\varepsilon}^2} \qquad (8)$$

Thus, the ω dependence of those data reflects the relaxation mode distribution determined by the global chain dynamics. Clearly, the mode distribution is different for the linear, star, and Cayley-tree PI chains, suggesting that the entanglement results in different types of global chain dynamics according to the chain architecture. In relation to this difference, experiments revealed that the dielectric mode distribution of linear PI is quite insensitive to M (*i.e.*, insensitive to a magnitude of entanglement) while that of star PI significantly broadens with increasing M_{arm}.[9,13,38] Furthermore, for respective PI samples examined in Figure 4, the mode distribution is broader for the viscoelastic relaxation than for the dielectric relaxation. This difference between the viscoelastic and dielectric mode distributions provides us with an important clue for analyzing the chain dynamics, as discussed later.

As noted from eq 7, $G'(\omega)$ and $G''(\omega)$ become proportional to ω^2 and ω, respectively, on a decrease of ω well below the relaxation frequency of the slowest mode, $1/\tau_{1;G}$. Similarly, $\varepsilon_0 - \varepsilon'(\omega)$ and $\varepsilon''(\omega)$ become proportional to ω^2 and ω at low $\omega \ll 1/\tau_{1;\varepsilon}$; *cf.* eq 8. These power-law type *terminal tails* are clearly noted in Figure 4, which indicates that the PI chains examined therein exhibit the global motion over their dimensions and fully relax at a lower-ω side in our experimental window.

The second-moment average viscoelastic and dielectric relaxation times are defined with respect to respective relaxation spectra as[9,13]

$$\langle \tau_G \rangle \equiv \frac{\sum\limits_{p\geq 1} h_{p;G} \tau_{p;G}^2}{\sum\limits_{p\geq 1} h_{p;G} \tau_{p;G}} = \left[\frac{G'(\omega)}{\omega G''(\omega)} \right]_{\omega\to 0} \qquad (9)$$

$$\langle \tau_\varepsilon \rangle \equiv \frac{\sum\limits_{p\geq 1} h_{p;\varepsilon} \tau_{p;\varepsilon}^2}{\sum\limits_{p\geq 1} h_{p;\varepsilon} \tau_{p;\varepsilon}} = \left[\frac{\varepsilon_0 - \varepsilon'(\omega)}{\omega \varepsilon''(\omega)} \right]_{\omega\to 0} \qquad (10)$$

These $\langle \tau \rangle$ are the averages heavily weighing on the slow relaxation modes and are close to τ_1 of the slowest relaxation mode. Thus, $\langle \tau_G \rangle$ and $\langle \tau_\varepsilon \rangle$ are utilized as the terminal viscoelastic and dielectric relaxation times. As shown in eqs 9 and 10, these $\langle \tau_G \rangle$ and $\langle \tau_\varepsilon \rangle$ are straightforwardly evaluated from the terminal tails explained above.

The $\langle \tau_G \rangle$ and $\langle \tau_\varepsilon \rangle$ data have been obtained for bulk monodisperse PI (with the polydispersity index < 1.1) with different architectures, linear PI without dipole inver-
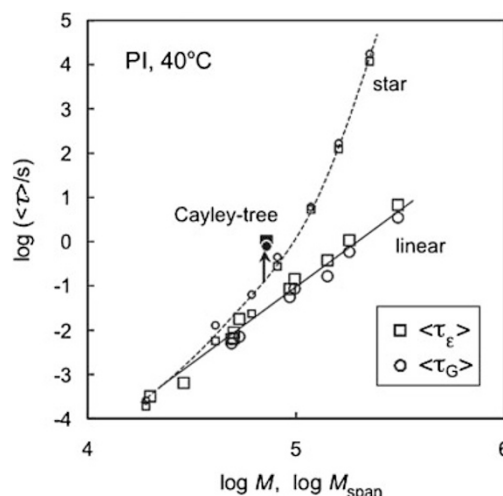

Figure 5. Terminal viscoelastic and dielectric relaxation times, $\langle \tau_G \rangle$ and $\langle \tau_\varepsilon \rangle$, obtained at 40 °C for bulk monodisperse PI (with the polydispersity index < 1.1) with different architectures, linear PI without dipole inversion,[27,35,38,40,41,43,44] regularly star-branched PI,[36–38,42,43] and Cayley-tree PI.[45] These data are plotted against the chain molecular weight M (for linear PI) and/or the span molecular weight M_{span} (for star and Cayley-tree PI). The data taken from refs 27, 35–38, and 40–45 with permission.

sion,[27,35,38,40,41,43,44] regularly star-branched PI,[36–38,42,43] and Cayley-tree PI[45] with the structure illustrated in the bottom panel of Figure 4. In Figure 5, the data obtained for entangled PI at 40 °C are plotted against the chain molecular weight M (for linear PI) and/or the span molecular weight M_{span} (for star and Cayley-tree PI). M_{span} is the molecular weight spanning the longest contour along the chain backbone; namely, $M_{span} = 2M_{arm}$ for the star PI and $M_{span} = 2M_{in} + 2M_{out}$ for the Cayley-tree type PI.

As noted in Figure 5, $\langle \tau_G \rangle$ (circle) and $\langle \tau_\varepsilon \rangle$ (square) are close to each other in magnitude, which confirms that the dielectric and viscoelastic relaxation detects the same global motion of the chain. We also confirm the well-known M dependence of $\langle \tau \rangle$ of entangled chains: $\langle \tau \rangle \sim M^\alpha$ with $\alpha \cong 3.5$ for linear PI (*cf.* solid line) and $\langle \tau \rangle \sim \exp(\nu' M_{arm}/M_e)$ with $\nu' \cong 0.7$ for star PI (*cf.* dotted curve). This difference of the M dependence as well as the difference of the magnitude of $\langle \tau \rangle$ of the linear and star chains (much larger for the star chain in the well-entangled regime) indicates that the branching point significantly retards the global motion of the star chain. In addition, $\langle \tau \rangle$ of the Cayley-tree PI chain (filled symbols) is even larger than $\langle \tau \rangle$ of the star PI chain having the same M_{span}, which confirms extra retardation of the global chain motion due to the outer branching point of the Cayley-tree chain.

Thus, the entangled chains of different architectures exhibit differences in their relaxation mode distribution (Figure 4) and terminal relaxation time (Figure 5). Molecular pictures for the global chain dynamics relevant to these differences are summarized below.

Molecular Picture of Fixed Tube for Entangled Chains

The entanglement effect undoubtedly results from the topological constraint due to uncrossability of the chains. The

Rouse-type equilibration rapidly occurs within each *entanglement segment* having the molecular weight M_e and thus the real chain can be coarse-grained as a sequence of these segments in the time scale of global relaxation.[9] This segment can be utilized as the motional unit in this time scale as well as the subchain in the expressions of the viscoelastic and dielectric relaxation functions, eqs 2 and 5.

The tube model proposed by Doi and Edwards[48–50] (DE) plays a central role even in the current molecular picture for the global relaxation of entangled chains. In the classical version of the tube model (including the DE model), the entanglement is regarded as a *spatially fixed* and uncrossable tube surrounding a chain of our focus. The tube diameter is taken to be identical to the entanglement segment size, a ($\propto M_e^{1/2}$). In this fixed tube model, the chain in the tube relaxes when it escapes the initial tube defined at time 0. Specifically, a linear chain is considered to relax through reptation (= curvilinear diffusion along the tube) and thermal contour length fluctuation (CLF; rather shallow fluctuation of the chain length measured along the tube),[51] and a star chain, through deep arm retraction (shrinkage of the star arm bringing its free end to the branching point).[52] The fixed tube model predicts exact coincidence of the normalized viscoelastic and dielectric relaxation functions, $\mu(t)$ and $\Phi(t)$ (*cf.* eqs 2 and 5), of type-A chains irrespective of their architecture, as can be easily noted from a simple analysis:[9,13,35,36] As explained for eq 1, the stress is essentially given as a product of the average orientational anisotropy of an entanglement segment (chosen as the subchain in eqs 2 and 5) and the total number of these segments. On imposition of a small step strain at time 0, the chain and the surrounding tube are affinely oriented so that all segments along the chain backbone have the same anisotropy on average. At a later time t, the initial anisotropy is perfectly preserved for the entanglement segments near the chain center/branching point remaining in the initial tube but lost for the other segments having escaped the tube. Thus, the average anisotropy for the segment at time t is given by the initial anisotropy multiplied by a fraction $\varphi(t)$ of the segments remaining in the initial tube, leading to a relationship $\mu(t) = \varphi(t)$. The orientational memory of a chain (at equilibrium) is also preserved for its portion(s) remaining in the initial tube but fully lost for the other portions having escaped the tube. Thus, $\Phi(t)$ also coincides with $\varphi(t)$, giving a relationship $\mu(t) = \Phi(t)$ irrespective of the details of the chain motion in the fixed tube. For the dynamic quantities examined in Figure 4, this fixed-tube relationship is cast in a form,

$$G'(\omega)/G_N = \{\varepsilon_0 - \varepsilon'(\omega)\}/\Delta\varepsilon, \quad G''(\omega)/G_N = \varepsilon''(\omega)/\Delta\varepsilon \quad (11)$$

The arm retraction (AR) mechanism considered in the fixed tube model for the star chain gives an entropic activation barrier for the chain motion, while the reptation and CLF mechanisms for the linear chain give no barrier. Correspondingly, this model can qualitatively explain the difference of the relaxation mode distribution and the terminal relaxation time of the star and linear chains.[9] However, the viscoelastic and dielectric data of monodisperse PI (Figure 4) do not obey the

fixed-tube relationship, eq 11, which unequivocally indicates that the tube for those chains, if any, is not fixed in space. Instead, the tube changes its shape according to the thermal motion of the tube-forming chains. The chain in the tube follows this tube motion thereby (partially) relaxing its orientational anisotropy. This mechanism of relaxation, referred to as thermal constraint release (CR),[8] has been confirmed from extensive experiments for binary blends of high- and low-M chains in which the high-M chains (probe) were dilute and entangled only with the low-M chains:[9,41–44] The viscoelastic terminal CR relaxation time τ_{CR} of the dilute probe was found to be well described by empirical equations, $\tau_{CR}/s = 1.0 \times 10^{-25} M_L^3 M_H^2$ (at 40 °C) for dilute linear probe PI in linear PI matrices[41,44] and $\tau_{CR}/s = 4.0 \times 10^{-5}\{M_H/M_e\}^2 \exp(0.71 M_L/M_e)$ (at 40 °C) for dilute star PI probe in star PI matrices,[42,43] where M_H and M_L are the molecular weights of the linear probe and matrix and/or the arm molecular weights of the star probe and matrix, respectively. The Rouse-CR model[8–10] considering random CR jumps of the probe segments over a distance a (the jumps activated by the matrix motion) is in harmony with these empirical equations. The observed CR relaxation mode distribution was close to prediction of the Rouse-type CR model as well, although a non-negligible difference related to the onset of the CR relaxation (requiring the full relaxation of the matrix chains) was also noted.[41–44]

The above empirical equations for τ_{CR} for blends can be extrapolated to monodisperse bulk linear and/or star PI by setting $M_L = M_H$ in these equations. This extrapolated τ_{CR} was found to be considerably longer than the actual terminal viscoelastic relaxation time $\langle\tau_G\rangle$ of monodisperse linear PI (for example, $\tau_{CR} \cong 30\langle\tau_G\rangle$ for $M = 30M_e$) while τ_{CR} for monodisperse star PI was rather close to $\langle\tau_G\rangle$ ($\tau_{CR} \cong 6\langle\tau_G\rangle$ for $M_{span} = 30M_e$).[43] Namely, the CR mechanism has an important contribution for the global relaxation not only in binary blends but also in monodisperse star systems.

Molecular Picture of Dynamic Tube Dilation (DTD) for Entangled Chains

As explained above, we need to combine at least the reptation, CLF, arm retraction (AR), and CR mechanisms if we utilize the tube model. This combination results in intractably complicated time-evolution equations of the relaxation functions that cannot be solved analytically.[53,54] For avoiding this complication, we may adopt a simplified but physically reasonable molecular picture proposed by Marrucci:[55] The CR mechanism allows the entanglement segment to jump in a lateral direction (perpendicular to the tube axis) over the tube diameter a, and accumulation of these CR jumps results in a lateral displacement much larger than a; see the top part of Figure 6 where small circles indicates the entanglement segments of a linear chain. However, in a given time scale t, this lateral CR displacement cannot exceed a certain spatial scale $a'(t)$, and the successive segments of the chain located within a spatial distance $a'(t)$ are mutually equilibrated (through exchange of their location) to behave as a larger, coarse-grained stress-sustaining unit explained earlier for eq 4.[9] This
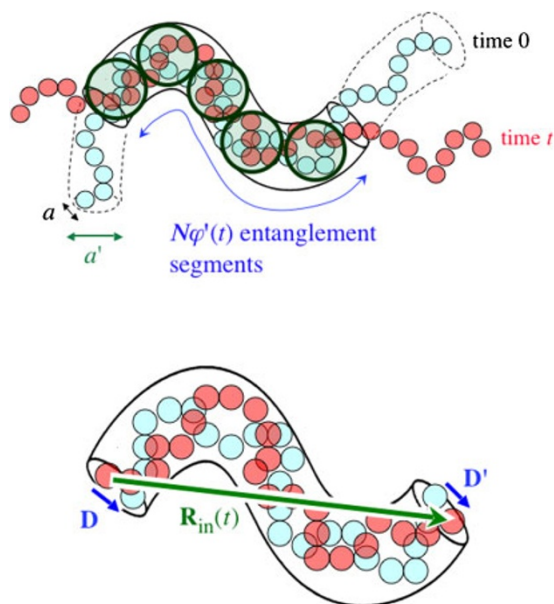
Figure 6. A schematic illustration of the dynamic tube dilation (DTD) mechanism.

unit, hereafter referred to a dilated segment, has the size $a'(t)$; see the large circles in the top part of Figure 6. Because of the Gaussian feature of the chain, the number of the segments that are CR-equilibrated, $\beta(t)$, is related to $a'(t)$ as

$$\beta(t) = \{a'(t)/a\}^2 \tag{12}$$

Since $a'(t)$ represents the upper bound of the lateral CR displacement in the given time scale t, the dilated segment is effectively constrained in a dilated tube of the diameter $a'(t)$ and move *only* along the axis of this tube. This molecular picture is referred to as *dynamic tube dilation* (DTD), because $a'(t)$ increases with increasing t (due to accumulation of the CR jumps).

The DTD picture is approximate because it smears details of the motion of the entanglement segments over a spatial scale $< a'(t)$. However, this picture incorporates the chain motion only along the dilated tube axis, which enables analytically tractable formulation of the relaxation functions. Thus, most of the refined tube models[55–60] adopt the DTD picture to effectively combine the CR motion with the reptation, CLF, and AR motion. The normalized viscoelastic relaxation function deduced from these refined models can be cast in a form,[9]

$$\mu(t) = \frac{\varphi'(t)}{\beta(t)} \tag{13}$$

Here, $\varphi'(t)$ is a fraction of the entanglement segments remaining in a hypothetical, initial dilated tube defined in the following way: The chain at time 0 is coarse-grained as a sequence of enlarged segments of the size $a'(t)$, and the hypothetical, initial dilated tube is defined as an envelope covering these enlarged segments; see top part of Figure 6. Note that eq 13 is straightforwardly deduced from eq 4:

From time 0 to t, the average orientational anisotropy of the enlarged segment decreases by a factor of $\varphi'(t)$, as similar to the situation in the fixed tube model explained earlier. In addition, in the DTD case, $\beta(t)$ entanglement segments as a whole behave as the stress-sustaining unit (dilated segment) at time t, giving a decrease of the number of these units by a factor of $1/\beta(t)$. These two kinds of decreases contribute to the relaxation of $\mu(t)$ thereby giving eq 13.

Within the DTD molecular picture, the dielectric relaxation function $\Phi(t)$ of the type-A chain can be related to the two DTD parameters, $\varphi'(t)$ and $\beta(t)$ (or $a'(t)$). Thus, we may utilize the $\Phi(t)$ data to determine $\varphi'(t)$ and test the DTD model. For this purpose, the relationship between $\Phi(t)$, $\varphi'(t)$ and $\beta(t)$ is derived below.

In the DTD molecular picture, the dielectric memory of a type-A chain is lost for the portions of the chain that have escaped the initial dilated tube. Thus, the dielectric $\Phi(t)$ is related to the auto-correlation of the end-to-end vector defined for the portion(s) remaining in the initial dilated tube. For example, for a linear chain that is composed of N entanglement segments and has non-inverted type-A dipoles, we can analyze the chain conformation at equilibrium in the following way. An inner portion of this chain remains in the initial dilated tube as illustrated in Figure 6, and $\Phi(t)$ of the chain (defined by eq 5 with $\xi(n) = 1$ for $n = 1 - N$) is expressed in terms of the end-to-end-vector $\mathbf{R}_{in}(t)$ of this portion as

$$\Phi(t) = \frac{\langle \mathbf{R}_{in}(t) \cdot \mathbf{R}_{in}(0) \rangle}{a^2 N} \tag{14}$$

As noted in the bottom part of Figure 6, $\mathbf{R}_{in}(t)$ at time t and $\mathbf{R}_{in}(0)$ at time 0 satisfy a relationship $\mathbf{R}_{in}(t) = \mathbf{R}_{in}(0) + \mathbf{D} + \mathbf{D}'$, where $\mathbf{D}$ indicates the displacement of an entanglement segment on one edge of the surviving part of the dilated tube in an interval of time from t to 0 and $\mathbf{D}'$ is the displacement of the other segment on the other edge in an interval from 0 to t. Since the inner portion of the chain contains $N\varphi'(t)$ entanglement segments (*cf.* top part of Figure 6) and behaves as a Gaussian chain to have $\langle R_{in}^2(0) \rangle = a^2 N \varphi'(t)$, eq 14 is rewritten as $\Phi(t) = \varphi'(t) + \langle \mathbf{R}_{in}(0) \cdot \{\mathbf{D}' + \mathbf{D}\} \rangle / a^2 N$.[40] Furthermore, from the equilibrium Gaussian feature at times 0 and t, $\langle \mathbf{R}_{in}(0) \cdot \mathbf{R}_{in}(0) \rangle = \langle \mathbf{R}_{in}(t) \cdot \mathbf{R}_{in}(t) \rangle$, we find a relationship $\langle \mathbf{R}_{in}(0) \cdot \mathbf{D}' \rangle = \langle \mathbf{R}_{in}(0) \cdot \mathbf{D} \rangle = -\langle D^2 \rangle / 2$. (The cross correlation $\langle \mathbf{D} \cdot \mathbf{D}' \rangle$ is small and negligibly contributes to this relationship, as suggested from the Rouse-CR analysis.[45]) The mean-square displacement $\langle D^2 \rangle$ is equivalent to a mean square separation of two entanglement segments randomly located on the same dilated tube edge of the diameter $a'(t)$ and calculated to be $\langle D^2 \rangle = \{a'(t) - a\}^2 / 4$.[40] Combining all these results with eqs 14 and 12, we finally obtain a relationship between $\Phi(t)$, $\varphi'(t)$, and $\beta(t)$,[40]

$$\Phi(t) = \varphi'(t) - \frac{1}{4N} [\{\beta(t)\}^{1/2} - 1]^2 \tag{15}$$

for linear chain without dipole inversion

The second term in the right-hand-side of eq 15 is a minor correction due to the segment displacement on the dilated tube

edge, and its contribution is almost negligible up to the dielectric terminal relaxation time $\langle \tau_\varepsilon \rangle$ (in particular for large N).[40] Namely, for the linear chain, the DTD mechanism itself only slightly accelerates the relaxation of dielectric $\Phi(t)$ compared to the dilated tube survival fraction $\varphi'(t)$, and $\Phi(t)$ essentially coincides with $\varphi'(t)$. The relationship between $\Phi(t)$, $\varphi'(t)$, and $\beta(t)$ has been derived also for star[42] and Cayley-tree[45] chains, and the results are very similar to eq 15 except that the numerical factor of 1/4 appearing therein is replaced by 1/8 and N is replaced by the entanglement number per arm (for star) and per inner arm plus outer arms grafted thereto (for Cayley tree). Thus, $\Phi(t)$ essentially coincides with $\varphi'(t)$ also for the star and Cayley-tree chains.

Test of Full-DTD Picture

Widely utilized DTD models[56–60] introduce an extra assumption that the relaxed portions of the chain (= portions having escaped the initial dilated tube) are equivalent to a solvent and the entanglement mesh size (= effective tube diameter) at time t fully dilates to the mesh size a_{sol} in a polymer solution having a concentration $c = \varphi'(t)$. These models, hereafter referred to as the *full-DTD* models, utilize the empirical relationship between a_{sol} and c for usual solutions, $a_{sol} \propto c^{-d/2}$ with $d = 1$–1.3 (dilation exponent; $d \cong 1.3$ for PI[40]), to express $\beta(t)$ and $\mu(t)$ (eq 13) in terms of $\varphi'(t)$ as

$$\beta_{\text{f-DTD}}(t) = \{\varphi'(t)\}^{-d}, \quad \mu_{\text{f-DTD}}(t) = \{\varphi'(t)\}^{1+d} \quad (16)$$

For the linear and star chains, respectively, the time evolution of $\varphi'(t)$ due to reptation/CLF and AR along the dilating tube has been formulated in the full-DTD model[57–59] to calculate $\mu_{\text{f-DTD}}(t)$. The tube length in this model, $L'(t) = \{N/\beta_{\text{f-DTD}}(t)\}a'(t) = Na\{\varphi'(t)\}^{d/2}$ with N being the number of the entanglement segments per linear chain/star arm, decreases with t and this decrease accelerates and broadens the relaxation of $\mu_{\text{f-DTD}}(t)$. (In particular, the acceleration due to DTD is significant for the star chain because the decrease of $L'(t)$ largely reduces the entropic barrier for AR.[56–58]) The calculated result agrees excellently with the viscoelastic data of monodisperse linear and star chains[57–60] (with an example shown later in Figure 8). Nevertheless, we should note that the viscoelastic relaxation detects just a limited aspect of the stochastic motion of the chains, *i.e.*, the decay of the orientational anisotropy, and thus this agreement does *not* necessarily guarantee the validity of the full-DTD picture for actual chains. We may utilize the dielectric data of PI chains to test this validity, as explained below.

In the full-DTD picture, $\beta(t)$ is expressed only in terms of $\varphi'(t)$; *cf.* eq 16. Then, eq 15 for linear PI and similar equations for star/Cayley-tree PI explained earlier become a closed equation(s) between $\varphi'(t)$ and $\Phi(t)$, which enables us to unequivocally evaluate $\varphi'(t)$ from the $\Phi(t)$ data. (The $\Phi(t)$ data are straightforwardly converted from the $\{\varepsilon_0 - \varepsilon'(\omega)\}/\Delta\varepsilon$ and $\varepsilon''(\omega)/\Delta\varepsilon$ data, for example, those shown in Figure 4.) Comparing the full-DTD prediction obtained from this $\varphi'(t)$, $\mu_{\text{f-DTD}}(t) = \{\varphi'(t)\}^{1+d}$ with $d \cong 1.3$ for PI[40] (eq 16), with the
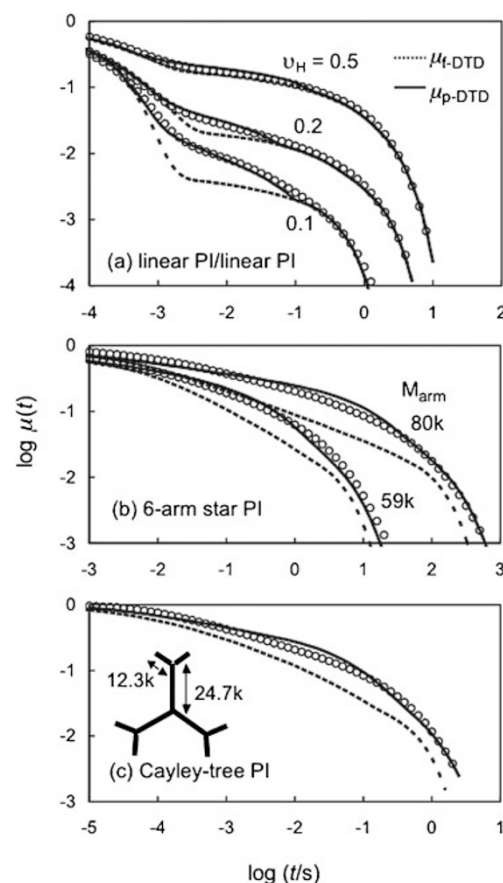

Figure 7. Normalized viscoelastic relaxation function $\mu(t)$ obtained at 40 °C for binary blends of linear PI with $M_H = 308 \times 10^3$ and $M_L = 21.4 \times 10^3$ (top panel),[40] monodisperse star PI with $M_{arm} = 59.0 \times 10^3$ and 80.1×10^3 (middle panel),[38] and Cayley-tree PI[45] of the structure as indicated (bottom panel). The dotted and solid curves indicate the viscoelastic relaxation function, $\mu_{\text{f-DTD}}(t)$ and $\mu_{\text{p-DTD}}(t)$, dielectrically evaluated for the cases of full-DTD and partial-DTD, respectively. The data taken from refs 38, 40, and 45 with permission.

$\mu(t)$ data of actual PI chains, we can test the full-DTD picture in an empirical and thus most reliable way.

In Figure 7, this comparison is made for binary blends of linear PI with the molecular weights $M_H = 308 \times 10^3$ and $M_L = 21.4 \times 10^3$ (top panel),[40] monodisperse star PI with the arm molecular weight $M_{arm} = 59.0 \times 10^3$ and 80.1×10^3 (middle panel),[38] and Cayley-tree PI[45] of the structure as indicated (bottom panel). The $\mu_{\text{f-DTD}}(t)$ expected for the full-DTD process are shown with the dotted curves, and the $\mu(t)$ data (straightforwardly converted from the $G'(\omega)/G_N$ and $G''(\omega)/G_N$ data) are shown with the circles. For the blend, $\mu_{\text{f-DTD}}(t)$ agrees well with the $\mu(t)$ data if the high-M chain therein has a large volume fraction, $\upsilon_H = 0.5$. Similar agreement was noted for monodisperse linear PI.[38,40,41] However, for the blends with smaller υ_H, $\mu_{\text{f-DTD}}(t)$ agrees with the $\mu(t)$ data only at short and long t (where the low-M and high-M chains exhibit respective terminal relaxation) and significant deviation is noted at intermediate t. For the star and Cayley-tree PI chains, $\mu_{\text{f-DTD}}(t)$ agrees with the $\mu(t)$ data only at short t and a
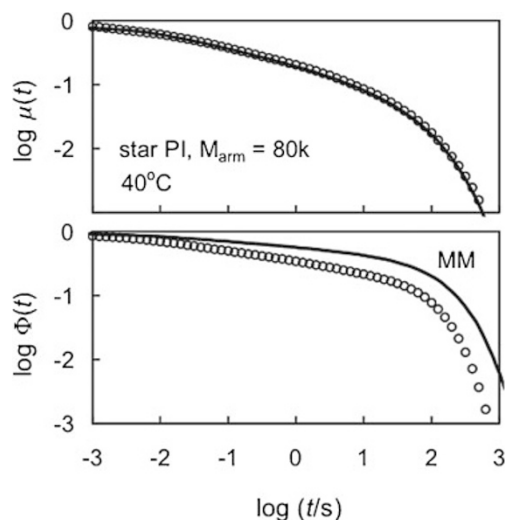
Figure 8. Comparison of the normalized viscoelastic and dielectric relaxation functions $\mu(t)$ and $\Phi(t)$ obtained for monodisperse star PI[38] with $M_{arm} = 80.1 \times 10^3$ (circles) with prediction of Milner-McLeish model based on the full-DTD molecular picture (solid curves). The data taken from ref 38 with permission.

significant deviation is noted in the dominant part of the terminal relaxation.

Thus, the full-DTD picture cannot consistently describe the dielectric and viscoelastic data for the blends with small υ_H and the monodisperse star/Cayley-tree chains. This failure of the full-DTD picture has been confirmed also for a sophisticated molecular model(s) assuming this picture. As an example, Figure 8 examines the full-DTD model for star chains proposed by Milner and McLeish (MM).[58] As seen in the top panel, the MM prediction with appropriately chosen model parameters (curve) excellently agrees with the viscoelastic $\mu(t)$ data of monodisperse star PI with $M_{arm} = 80.1 \times 10^3$ (circles).[38] However, the prediction based on the same model parameters significantly deviate from for the dielectric $\Phi(t)$ data, as shown in the bottom panel.[38] It has been also confirmed that a moderate adjustment of the parameters allows the model to well describe the $\Phi(t)$ data but leads to a significant deviation from the $\mu(t)$ data.[42] Namely, the full-DTD model cannot consistently describe the viscoelastic and dielectric data.

Test of Partial-DTD Picture

Since the successive entanglement segments are undoubtedly equilibrated through their CR motion, the DTD picture describing this CR-equilibration on a coarse-grained level has a sound physical basis. Thus, the failure of the full-DTD picture explained in the previous section should result from the extra full-DTD assumption that the number of the mutually equilibrated segment is always given by that in the corresponding solution, $\beta_{f\text{-DTD}}(t) = \{\varphi'(t)\}^{-d}$ (eq 16). Since the actual CR-equilibration *can* occur only for a given number $\beta_{CR}(t)$ of segments and this $\beta_{CR}(t)$ is determined by the CR mechanism itself, the full-DTD picture naturally fails in a time scale where $\beta_{CR}(t)$ is smaller than $\beta_{f\text{-DTD}}(t)$. In other words, the

failure of the full-DTD picture is expected to result from inconsistent coarse-graining of the length and time scales that leads to over-estimation of $\beta(t)$. This expectation is examined below.

The CR-equilibration number $\beta_{CR}(t)$ can be estimated from the empirical equations for the terminal viscoelastic CR time τ_{CR} explained earlier with the aid of the Rouse-CR model. In this model, the coarse-graining of the entanglement segments occurs uniformly along the chain backbone, and its relaxation function $\psi_{CR}(t)$ is equivalent to a ratio of the number of the coarse-grained (dilated) segments at time t to the number of the entanglement segments. Thus, within the context of the Rouse-CR model, $\beta_{CR}(t)$ is estimated as

$$\beta_{CR}(t) = 1/\psi_{CR}(t) \tag{17}$$

The functional form of $\psi_{CR}(t)$ is determined according to the architecture of the chain. For example, for the star chain having N entanglement segments per arm, $\psi_{CR}(t)$ can be formulated as the Rouse-CR relaxation function for a tethered chain:[43]

$$\psi_{CR}(t) = \frac{1}{N}\left[\sum_{p=1}^{N-N_f} \exp\left(-\frac{r_p t}{2\tau_{CR}}\right) + \sum_{q=1}^{N_f} \exp\left(-\frac{r'_q t}{\tau_f}\right)\right] \tag{18}$$

Here, the factor $2\tau_{CR}$ represents the terminal dielectric CR time, and τ_f and $N_f (\cong N^{1/2})$ denote the longest relaxation time for the contour length fluctuation (CLF) of the tethered chain (star arm) and the number of entanglement segments corresponding to the CLF amplitude, respectively. (The second summation represents the CLF contribution to the Rouse-CR relaxation.) The factor r_p is the ratio of τ_{CR} to the characteristic time of p-th viscoelastic CR mode, and the factor r'_q is the ratio of τ_f to the relaxation time of q-th CLF mode. These ratios are given by[43]

$$r_p = \sin^2\left(\frac{\pi\{2p-1\}}{2\{2N+1\}}\right) \sin^{-2}\left(\frac{\pi}{2\{2N+1\}}\right) \tag{19}$$

and

$$r'_q = \sin^2\left(\frac{\pi\{2q-1\}}{2\{2N_f+1\}}\right) \sin^{-2}\left(\frac{\pi}{2\{2N_f+1\}}\right) \tag{20}$$

For comparison of $\beta_{CR}(t)$ and $\beta_{f\text{-DTD}}(t)$ for the monodisperse star PI chains examined in Figure 7, τ_{CR} was evaluated from the empirical equation rewritten for those chains,[42,43] $\tau_{CR}/s = 4.0 \times 10^{-5}\{M_{arm}/M_e\}^2 \exp(0.71M_{arm}/M_e)$ at $40\,^\circ$C, and τ_f was estimated as the terminal dielectric relaxation time of non-entangled linear PI described by an empirical equation, $\langle\tau_\varepsilon\rangle/s = 9.3 \times 10^{-13}M^2$ at $40\,^\circ$C.[43] These τ_{CR} and τ_f values were utilized in eq 18 to evaluate $\psi_{CR}(t)$ for the star PI. The corresponding $\beta_{CR}(t)$ ($= 1/\psi_{CR}(t)$) was found to be considerably smaller than $\beta_{f\text{-DTD}}(t)$ (eq 16) in the range of t where failure of the full-DTD picture was observed in the middle panel of Figure 7. This result confirms the expectation that this failure results from the inconsistent coarse-graining of the length and time scales. The same conclusion was obtained for the failure of the full-DTD picture for the PI blends[40,41] and the Cayley-tree PI[45] examined in Figure 7. It turned out that the branched chains exhibit intensive fast relaxation modes due to

the hierarchical relaxation (from the outer end of the arm toward the inner branching point) and a very rapid increase of $\beta_{\text{f-DTD}}(t)$ due to these fast modes cannot be followed by the actual Rouse-CR motion of the entanglement segments.[38,42,45] Similarly, in the blends, intensive fast relaxation of the low-M chain leads to a very rapid increase of $\beta_{\text{f-DTD}}(t)$ that cannot be immediately followed by the actual Rouse-CR motion.[40,41]

The above results in turn suggest that we can coarse-grain the length and time scales consistently to formulate the DTD model in a sound form,[41]

$$\mu_{\text{p-DTD}}(t) = \frac{\varphi'(t)}{\beta^*(t)} \quad \text{with} \quad \beta^*(t) = \min[\beta_{\text{f-DTD}}(t), \beta_{\text{CR}}(t)]$$

(21)

Eq 21 simply considers that the tube dynamically dilates to a level allowed by the CR mechanism: If $\beta_{\text{f-DTD}}(t) < \beta_{\text{CR}}(t)$, the tube actually dilates to a level assumed in the full-DTD picture and $\beta_{\text{f-DTD}}(t)$ entanglement segments are CR-equilibrated to behave as the dilated segment. On the other hand, if $\beta_{\text{f-DTD}}(t) > \beta_{\text{CR}}(t)$, the tube dilates to the maximum possible level allowed by the CR mechanism and $\beta_{\text{CR}}(t)$ segments behave as the dilated segment. This molecular picture is referred to as *partial-DTD* picture.[41]

The $\varphi'(t)$ and $\beta_{\text{f-DTD}}(t)$ for the full-DTD picture have been obtained in the test of this picture explained in the previous section. The $\beta_{\text{CR}}(t)$ has been estimated as reciprocal of the Rouse-CR relaxation function $\psi_{\text{CR}}(t)$ (*cf.* eq 18 for star chain). The $\varphi'(t)$ for the case of $\beta^*(t) = \beta_{\text{CR}}(t) < \beta_{\text{f-DTD}}(t)$ is simply evaluated from the dielectric $\Phi(t)$ data with the aid of eq 15 for a linear chain and similar equations for the star/Cayley-tree chains explained earlier: On replacement of $\beta(t)$ appearing in these equations by the known $\beta_{\text{CR}}(t)$ ($= 1/\psi_{\text{CR}}(t)$), the equations become closed equations between $\varphi'(t)$ and $\Phi(t)$ so that $\varphi'(t)$ is straightforwardly evaluated from the $\Phi(t)$ data. Thus, all parameters included in the partial-DTD picture are experimentally determined, and the partial-DTD picture can be tested accordingly.

In Figure 7, $\mu_{\text{p-DTD}}(t)$ for this picture (eq 21) is shown with the solid curves. In the range of t where the solid curves are superposed on the dotted $\mu_{\text{f-DTD}}(t)$ curves, $\beta_{\text{f-DTD}}(t)$ is smaller than $\beta_{\text{CR}}(t)$ and the partial-DTD picture reduces to the full-DTD picture. Clearly, $\mu_{\text{p-DTD}}(t)$ agrees with the $\mu(t)$ data (circles) satisfactorily in the entire range of t. This result lends strong support to the simple partial-DTD picture thereby demonstrating the importance of the consistency in the coarse-graining of the length and time scales (as incorporated in this picture).

In relation to this result, we should emphasize that the partial-DTD picture formulated as above just gives a relationship between the viscoelastic and dielectric data on the basis of the self-consistent coarse-graining. In other words, this picture does not specify details of the chain motion in the dilating tube and the corresponding time evolution of the viscoelastic and dielectric relaxation functions. This specification requires a sophisticated model that explicitly combines the reptation, CLF, and AR mechanisms in the consistently coarse-grained length and time scales. Larson and coworkers[61] and van

Ruymbeke and coworkers[62,63] formulated the DTD models incorporating this concept of consistent coarse-graining, but the predictions of the current models do not appear to agree satisfactorily with the viscoelastic and dielectric data. Their models may serve as a good starting point for further refinement of the DTD model.

SLOW DYNAMICS AT EQUILIBRIUM: EIGEN-MODE ANALYSIS

As clearly noted from eqs 2 and 5, the viscoelastic and dielectric data of polymers detect the orientational anisotropy and the orientational memory *averaged* for all constituent subchains. These averages are useful for the analysis of coarse-graining presented in the previous section but do not allow us to resolve further detail of the intra-chain dynamics (reflecting the motion of individual subchains). This resolution requires us to introduce a partial label to the chains. For example, dichroism experiments for partially deuterium-labeled chains can detect orientational relaxation of the labeled portion of the chain, and comparison of the relaxation rates of several portions provides us with a clue for resolving the intra-chain motion, for example, the relaxation faster for the chain end than for the chain center.[64,65] (The deuterium-label is also useful for resolving the component chain dynamics in blends[66] and for analyzing the welding behavior.[67])

The type-A dipole can be also utilized as a label. For example, a copolymer composed of miscible blocks of PI and poly(vinyl ethylene) (PVE) allows us to selectively observe the motion of the type-A PI block in a long time scale, because PVE has no type-A dipole and its motion is dielectrically active only in the segmental relaxation regime at short times.[68] However, the segmental friction coefficient is different even for the chemically similar PI and PVE blocks in the miscible state. Thus, the use of the dipole-labeled block copolymer does not allow us to rigorously investigate the dynamics of the corresponding homopolymers.

However, we can still investigate the intra-chain dynamics of type-A homopolymers by introducing inversion of the type-A dipoles. Namely, the dipole-inversion serves as a label to resolve the intra-chain eigenmodes. In fact, a series of PI chains having symmetrically[17,27,31] and asymmetrically[27] once-inverted type-A dipoles has been synthesized with an anionic coupling method, and their eigenmodes have been experimentally resolved.[27–33] Furthermore, viscoelastic moduli expected from the dielectrically determined eigenmodes have been compared with the moduli data to specify coherence of the intra-chain dynamics.[28,30,33] The results are summarized below.

Eigenmodes of Linear Chain in Bulk

Top panel of Figure 9 shows the dielectric loss ε'' measured for a series of seven dipole-inverted bulk PI samples having nearly the same molecular weights ($10^{-3}M = 48.8$, 55.4, 44.4, 47.6, 48.9, 47.4, and 47.7) but different locations of the dipole inversion, $n^*/N = 0$, 0.109, 0.213, 0.283, 0.325, 0.396, and 0.5 with n^* being the subchain (segment) index of the dipole
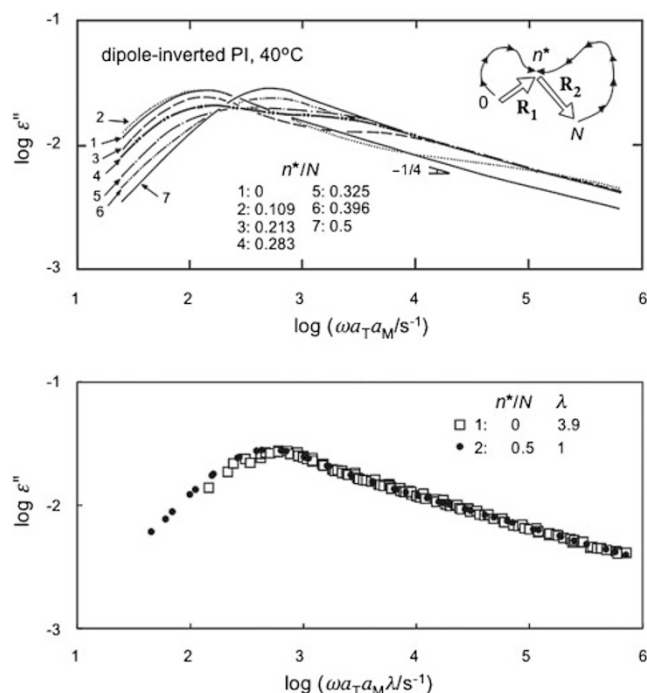
Figure 9. Top panel: Dielectric loss ε'' obtained at 40 °C for a series of seven dipole-inverted bulk PI samples having nearly the same molecular weights ($10^{-3}M = 48.8$, 55.4, 44.4, 47.6, 48.9, 47.4, and 47.7) but different locations of the dipole inversion (see illustration), $n^*/N = 0$, 0.109, 0.213, 0.283, 0.325, 0.396, and 0.5 with n^* being the subchain index of the dipole inversion point and N being the total number of subchains per chain.[27] The polydispersity index is smaller than 1.1 for all samples. **Bottom panel**: Comparison of $\varepsilon''(\omega)$ data of the samples 1 and 7 examined in the top panel. The data for the sample 1 (having no inversion of type-A dipoles) are shifted to higher frequency by a factor of $\lambda = 3.9$. The data taken from ref 27 with permission.

inversion point and N being the total number of subchains per chain;[27] see the illustration therein. (To avoid heavy overlapping of the data points, curves smoothly connecting the data points are shown.) The sample 1 has no inversion of the dipole ($n^*/N = 0$), while the sample 7 has the symmetrical inversion ($n^*/N = 0.5$). The polydispersity index is smaller than 1.1 for all samples. The samples have $M \cong 10M_e$ and are in the well entangled state to exhibit the terminal viscoelastic relaxation time $\langle \tau_G \rangle \propto M^{3.5}$. The $\varepsilon''(\omega)$ data are double-logarithmically plotted against a reduced frequency $\omega a_T a_M$, where a_T is the time-temperature superposition shift factor (identical for all samples) and a_M is a correction factor for minor differences of $\langle \tau_G \rangle$; $a_M = (M/47.7 \times 10^3)^{3.5}$ where the sample 7 having $M = 47.7 \times 10^3$ has been chosen as a reference for this correction. Thus, we can regard the chain dynamics to be exactly the same for the seven samples in the plots shown here. Nevertheless, the dielectric behavior is quite different for those samples. This difference results from the dipole inversion serving as a label for the intra-chain eigenmodes, as explained below.

For the PI chain with the dipole inversion at n^*-th subchain, the dipole index $\xi(n)$ appearing in eq 5 has a value, $\xi(n) = 1$ for $0 < n < n^*$ and $\xi(n) = -1$ for $n^* < n < N$. Thus, the normalized dielectric relaxation function $\Phi(t; n^*)$ of this PI chain can be expressed in terms of the local correlation

function, $C(n, t; m) = a^{-2} \langle \mathbf{u}(n, t) \cdot \mathbf{u}(m, 0) \rangle$ with $\mathbf{u}(n, t)$ and a being the bond vector of n-th subchain at time t and the subchain size at equilibrium, as (*cf.* eq 5)

$$\Phi(t; n^*) = \frac{1}{N} \left[\int_0^{n^*} \mathrm{d}n - \int_{n^*}^N \mathrm{d}n \right] \left[\int_0^{n^*} \mathrm{d}m - \int_{n^*}^N \mathrm{d}m \right] C(n, t; m) \tag{22}$$

where the subchain index n has been regarded as a continuous variable running from 0 to N and the summation in eq 5 has been replaced by an integral. The local correlation function appearing in eq 22 can be expanded with respect to its eigenmodes as[27]

$$C(n, t; m) = \frac{2}{N} \sum_{p=1}^N f_p(n) f_p(m) \exp\left(-\frac{t}{\tau_p}\right) \tag{23}$$

where $f_p(n)$ and $1/\tau_p$ ($p = 1, 2, \ldots, N$) are the eigenfunctions and eigenvalues associating to this function, as explained later in more detail. From eqs 22 and 23 together with a general expression of ε'', eq 8, the $\varepsilon''(\omega; n^*)$ data of PI having the dipole inversion at n^*-th subchain can be expressed as

$$\varepsilon''(\omega; n^*) = \Delta\varepsilon \sum_{p \geq 1} h_{p;\varepsilon}(n^*) \frac{\omega \tau_p}{1 + \omega^2 \tau_p^2} \tag{24}$$

with

$$h_{p;\varepsilon}(n^*) = \frac{2}{N^2} \left[\int_0^{n^*} f_p(n)\mathrm{d}n - \int_{n^*}^N f_p(n)\mathrm{d}n \right]^2$$
$$= [2F_p(n^*) - F_p(N)]^2 \tag{25}$$

where $F_p(n)$ is an integrated eigenfunction defined by

$$F_p(n) = \frac{\sqrt{2}}{N} \int_0^n f_p(n')\mathrm{d}n' \quad (= 0 \text{ for } n = 0) \tag{26}$$

Eq 25 clearly indicates that the normalized dielectric intensity $h_{p;\varepsilon}(n^*)$ changes with n^*, although the chain dynamics is identical for the samples 1–7. This change is observed as the difference of the $\varepsilon''(\omega)$ data of those samples in the top panel of Figure 9.

In the top panel of Figure 9, we also note that the shape of the $\varepsilon''(\omega)$ curve is very similar for the sample 1 having no dipole inversion and the sample 7 having the symmetrical inversion. In fact, the $\varepsilon''(\omega)$ data of the sample 1 plotted against a shifted frequency $\omega a_T a_M \lambda$ with $\lambda = 3.9$ are indistinguishable from the data of the sample 7 plotted against the non-shifted frequency $\omega a_T a_M$, as shown in the bottom panel. This result allows us to find a characteristic feature of $h_{p;\varepsilon}(n^*)$ and $1/\tau_p$, as discussed below.

The eigenfunctions $f_p(n)$ are classified into odd and even functions being symmetrical and anti-symmetrical with respect to the chain center ($n = 1/2$); $f_p(n) = f_p(N - n)$ and $f_p(n) = -f_p(N - n)$ for $p = $ odd and even, respectively. Thus, only the odd eigenfunctions contribute to the dielectric intensity of the sample 1 having $n^* = 0$ (*i.e.*, $h_{p;\varepsilon}(0) = 0$ for $p = $ even), while only the even eigenfunctions contribute to the dielectric intensity of the sample 7 having $n^* = N/2$ ($h_{p;\varepsilon}(N/2) = 0$ for $p = $ odd), as can be noted from eq 25. Correspondingly, the coincidence of the $\varepsilon''(\omega)$ data of the samples 1 and 7 strongly
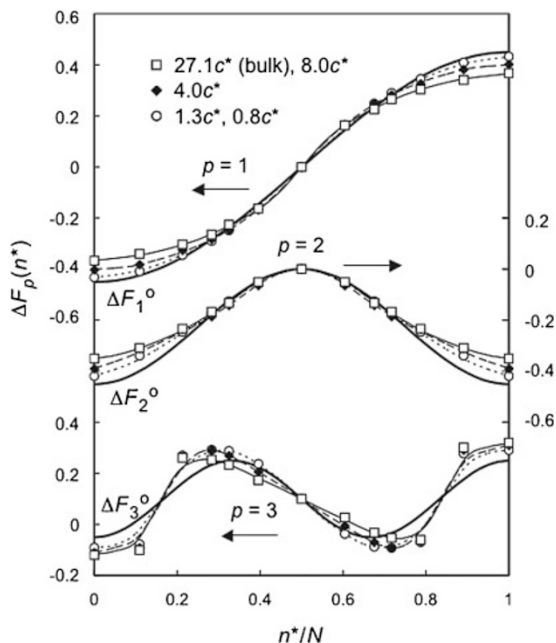
Figure 10. Integrated and shifted eigenfunctions for the lowest three eigenmodes, $\Delta F_p(n^*) \equiv F_p(n^*) - F_p(N/2)$ with $p = 1$–3, dielectrically determined for a series of dipole-inverted PI chains examined in Figure 9. The $\Delta F_p(n^*)$ data were obtained for the PI bulk/solutions in oligomeric butadiene ($M = 700$) at PI concentrations[27,29] $c = 27.1c^*$ (bulk system), $8.0c^*$, $4.0c^*$, $1.3c^*$, and $0.8c^*$. Solid curves indicate sinusoidal eigenfunctions, $\Delta F_p^o(n^*) = (\sqrt{2}/p\pi)\{\cos(p\pi/2) - \cos(p\pi n^*/N)\}$, deduced from the reptation/Rouse-CR model as well as the Zimm model. The data taken from ref 27 and 29 with permission.

suggests that the dielectric intensity $h_{1;\varepsilon}$ and the eigenvalue $1/\tau_1$ of the slowest eigenmode and $h_{2;\varepsilon}$ and $1/\tau_2$ of the second-slowest eigenmode satisfy relationships, $h_{1;\varepsilon}(0) = h_{2;\varepsilon}(N/2)$ and $\tau_1/\tau_2 = 3.9$.

On the basis of eq 24, we can decompose the $\varepsilon''(\omega; n^*)$ data of the dipole-inverted bulk PI chains into the contributions from respective eigenmodes to evaluate their $1/\tau_p$ and $h_{p;\varepsilon}(n^*)$, the latter being obtained as a function of n^*.[27] Actually, this evaluation was made with satisfactory accuracy for the lowest three eigenmodes with $p = 1$, 2, 3, giving a ratio of $\tau_1:\tau_2:\tau_3 = 1:1/3.9:1/7.4$.[27] This ratio was close to that deduced from a model combining the reptation and Rouse-CR mechanisms ($\tau_1:\tau_2:\tau_3 = 1:1/4:1/9$).[27] However, a deviation from this model was noted for the integrated eigenfunctions $F_p(n^*)$ evaluated from $h_{p;\varepsilon}(n^*)$ (*cf.* eqs 25 and 26): In Figure 10, $\Delta F_p(n^*) \equiv F_p(n^*) - F_p(N/2)$ obtained for bulk PI is plotted against n^*/N; see squares. The prediction of the reptation/Rouse-CR model, $\Delta F_p^o(n^*) = (\sqrt{2}/p\pi)\{\cos(p\pi/2) - \cos(p\pi n^*/N)\}$ shown with the solid curves, considerably deviate from the $\Delta F_p(n^*)$ data. In particular, at around the chain ends ($n^* \cong 0$ and N), the $\Delta F_p(n^*)$ data is less dependent on n^* compared to the model $\Delta F_p^o(n^*)$. Since the eigenfunction $f_p(n)$ is obtained as a derivative $\{N/\sqrt{2}\}d\Delta F_p(n)/dn$ (*cf.* eq 26), this observation indicates that $f_p(n)$ of actual PI chains is smaller, in magnitude, compared to the model $f_p^o(n)$ at $n \cong 0$ and N. The difference of the ω dependence of the ε'' data ($\varepsilon'' \propto \omega^{-1/4}$ at high ω; see top panel of Figure 9) and the model

prediction ($\varepsilon'' \propto \omega^{-1/2}$) can be related to this difference of the eigenfunctions.[27]

The above result indicates that the dynamics of actual PI chains is not accurately described by the reptation/CR-Rouse model. In relation to this fact, it is informative to analyze the time evolution equation for the local correlation function $C(n, t; m)$ deduced from this model,

$$\frac{\partial}{\partial t} C(n, t; m) = \frac{1}{\tau_1^o}\left(\frac{N}{\pi}\right)^2 \frac{\partial^2}{\partial n^2} C(n, t; m) \qquad (27)$$

where τ_1^o is the longest relaxation time of $C(n, t; m)$. In the model, τ_1^o is given by a harmonic average of the reptation and Rouse relaxation times.[9] (Note also that τ_1^o is identical to the dielectric $\tau_{1;\varepsilon}$ of the chain without dipole inversion.) The boundary condition representing instantaneous decay of orientational memory at the chain ends is given by

$$C(n, t; m) = 0 \text{ for } n = 0, N \text{ and } m = 0, N \qquad (28)$$

The eigenfunction equation associating eq 27 is written as

$$\frac{1}{\tau_p} f_p^o(n) = -\frac{1}{\tau_1^o}\left(\frac{N}{\pi}\right)^2 \frac{d^2}{dn^2} f_p^o(n) \quad \text{with}$$
$$f_p^o(n) = 0 \text{ for } n = 0, N \qquad (29)$$

This equation is easily solved to give $1/\tau_p = p^2/\tau_1^o$ and $f_p^o(n) = \sin(p\pi n/N)$, and $C(n, t; m)$ is expressed in the form of eq 23 satisfying the Gaussian feature, $C(n, 0; m) = \delta_{nm}$. At $n \cong 0$ and N, the observed $f_p(n)$ is smaller, in magnitude, compared to the model $f_p^o(n)$, as explained for Figure 10. As judged from this fact as well as the close coincidence of the τ_p ratio ($\tau_1:\tau_2:\tau_3 = 1:1/3.9:1/7.4$ and $1:1/4:1/9$ for the experiment and model, respectively), the actual eigenfunctions $f_p(n)$ is possibly affected by an extra relaxation mechanism (in addition to reptation and Rouse-CR) and described by[27]

$$\frac{1}{\tau_p} f_p(n) = -\frac{1}{\tau_1^o}\left(\frac{N}{\pi}\right)^2 \frac{d^2}{dn^2} f_p(n) + U(n)f_p(n) \quad \text{with}$$
$$f_p(n) = 0 \text{ for } n = 0, N \qquad (30)$$

Here, $U(n)$ represents the effect of the extra mechanism on $f_p(n)$. Eq 30 is formally identical to the Schrödinger equation for a particle subjected to a hard-core potential at $n < 0$ and $n > N$ as well as a soft potential $U(n)$ at $0 < n < N$, and $\{f_p(n)\}^2$ is analogous to the probability density. With this analogy, we can easily note that the probability density decreases, *i.e.*, $f_p(n)$ is smaller in magnitude compared to $f_p^o(n)$, at $n \cong 0$ and N if $U(n)$ is larger at $n \cong 0$ and N than at $n \cong N/2$. Thus, the extra relaxation mechanism (represented by U) being enhanced at around the chain ends appears to distort the eigenfunction from $f_p^o(n)$ toward the observed $f_p(n)$.

This extra mechanism could be the contour length fluctuation (CLF) and/or the non-localized CR:[27] In the non-localized CR mechanism, a CR jump at around the chain center can result in a change in the chain tension, and this change can be rapidly transmitted to the chain end through the intrinsic Rouse motion along the chain backbone thereby activating the motion of the chain ends.[9] However, no further details of the mechanism have been elucidated, and a further study is desired.
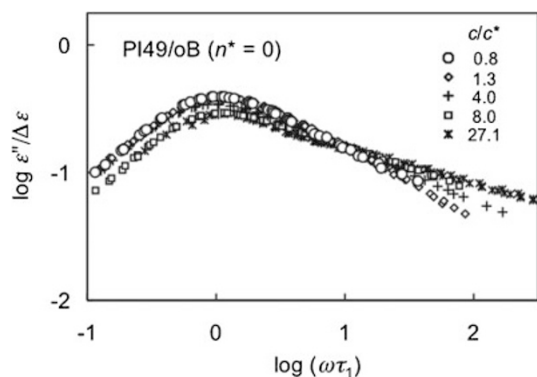
Figure 11. Normalized dielectric loss, $\varepsilon''(\omega)/\Delta\varepsilon$, measured for linear PI without dipole inversion ($M = 48.8 \times 10^3$; sample 1 examined in Figure 9) dissolved in an oligomeric butadiene ($M = 700$).[29] The PI concentrations are $27.1c^*$ (in bulk system), $8.0c^*$, $4.0c^*$, $1.3c^*$, and $0.8c^*$. The data are plotted against a reduced frequency, $\omega\tau_{1;\varepsilon}$, with $\tau_{1;\varepsilon}$ being the longest dielectric relaxation time. The data taken from ref 29 with permission.

Eigenmodes of Linear Chain in Solution

For the PI samples examined in Figure 9, the dielectric behavior has been examined not only in bulk state but also in solutions.[29,30] As an example, Figure 11 shows the normalized dielectric loss, $\varepsilon''(\omega)/\Delta\varepsilon$, measured for the PI sample 1 ($M = 48.8 \times 10^3$; without dipole inversion) dissolved in an oligomeric butadiene (oB; $M = 700$).[29] The PI concentrations are $c/\text{g cm}^{-3} = 0.92$ (in bulk state), 0.272, 0.135, 0.045, and 0.027, and the corresponding degrees of overlapping are given by $c/c^* = 27.1$, 8.0, 4.0, 1.3, and 0.8, respectively. The data are plotted against a reduced frequency, $\omega\tau_{1;\varepsilon}$, with $\tau_{1;\varepsilon}$ being the longest dielectric relaxation time (evaluated by decomposing the ε'' data into contributions from the eigenmodes, as done for bulk systems). Clearly, the dielectric mode distribution narrows on dilution below a certain concentration, $c \sim 4c^*$, and appears to converge to the distribution at infinite dilution on the decrease of c below $1.3c^*$. Similar behavior was observed for the solutions of the other PI samples 2–7 having different locations of the dipole inversion.[29]

The dielectric data of those PI/oB solutions were subjected to the analysis explained in the previous section to determine the eigenvalues $1/\tau_p$ and integrated eigenfunctions $F_p(n^*)$ for $p = 1$–3. The τ_p spacing, $\tau_1:\tau_2:\tau_3$, was found to narrow a little on dilution, from $1:1/3.9:1/7.4$ for $c = 27.1c^*$ (bulk) to $1:1/3.4:1/6.8$ for $c = 0.8c^*$.[29] However, this change of the τ_p was just a minor factor contributing to the narrowing of the $\varepsilon''(\omega)/\Delta\varepsilon$ curve on dilution (Figure 11). Instead, the eigenfunctions determining the dielectric mode intensities $h_{p;\varepsilon}$ were found to change their functional forms thereby governing this narrowing of the $\varepsilon''(\omega)/\Delta\varepsilon$ curve: This change is demonstrated in Figure 10 where the integrated and shifted eigenfunctions $\Delta F_p(n^*) \equiv F_p(n^*) - F_p(N/2)$ (with $F_p(n^*)$ being evaluated from the $h_{p;\varepsilon}(n^*)$ data; cf. eq 25) are shown for the PI solutions with various c. $\Delta F_p(n^*)$ for $c = 8.0c^*$ is very close to that for $c = 27.1c^*$ (see squares), and $\Delta F_p(n^*)$ for $c = 1.3c^*$ is

indistinguishable from that for $c = 0.8c^*$ (see circles). On dilution, the $\Delta F_p(n^*)$ data approach the sinusoidal $\Delta F_p^o(n^*) = (\sqrt{2}/p\pi)\{\cos(p\pi/2) - \cos(p\pi n^*/N)\}$ (solid curves) deduced from not only the reptation/Rouse-CR model but also the Zimm model,[69,70] the latter being established for dilute polymer solutions. This change of the eigenfunctions and the corresponding narrowing of the dielectric modes can be mainly attributed to disappearance of some inter-chain topological interaction on dilution.[29]

Here, a comment needs to be added for this topological interaction. One may argue that the disappearance of entanglement on dilution is mainly responsible for the change of the eigenfunctions and the dielectric mode narrowing on dilution. However, this is not the case, as evidenced from a fact that the slow dielectric mode distribution of bulk PI *never* exhibits the narrowing even when the molecular weight is decreased below M_e.[9,13] Instead, the inter-chain topological interaction responsible for the dielectric mode narrowing appears to be the local motional cooperativity of densely packed polymer chains at length scales smaller than the entanglement spacing ($\propto M_e^{1/2}$). The packing of the polymer chains should be loosened by the low-M solvent and the local cooperativity would be reduced accordingly, which possibly results in the narrowing. This argument is in harmony with an observation that the dipole-inverted PI samples examined in Figures 9–11 exhibited no narrowing of their dielectric modes in miscible blends with a polymeric PB matrix even when their concentration was small ($c \cong 1.3c^*$).[28]

Coherence of Subchain Motion

Viscoelastic and dielectric properties of type-A polymers are equivalent to the orientational anisotropy and the orientational memory averaged over all subchains in the system, as explained earlier. Thus, starting from an equation of motion (Langevin equation) for the subchain and comparing these properties, we may analyze detailed feature of the intra-chain dynamics, coherence of the subchain motion. In fact, this analysis has been made.[30,33] The results are summarized below. (It should be noted that this approach makes no coarse-graining and thus different, in a fundamental standing point, from the DTD analysis explained earlier.)

For a linear chain composed of N subchains, we consider the dynamics at equilibrium. In general, the time evolution of the bond vector of n-th subchain, $\mathbf{u}(n, t)$, can be described by a Langevin equation of a form,[28]

$$\mathbf{u}(n, t + \Delta t) = \mathcal{L}^*(n; \Delta t)\mathbf{u}(n, t) + \int_t^{t+\Delta t} \frac{1}{\zeta}\frac{\partial}{\partial n}\mathbf{F}_B(n, t')dt' \quad (31)$$

Here, $\mathcal{L}^*(n; \Delta t)$ ($= 1$ for $\Delta t = 0$) is an operator for $\mathbf{u}$ at time t, ζ is the subchain friction, and $\mathbf{F}_B(n, t)$ denotes a random thermal force acting on the n-th segment at time t. The functional form of $\mathcal{L}^*$ is determined according to the chain dynamics, and the operation $\mathcal{L}^*\mathbf{u}$ may involve both local and nonlocal operations.[28] From eq 31, the time evolution equation for the local correlation function, $C(n, t; m) = a^{-2}\langle\mathbf{u}(n, t) \cdot \mathbf{u}(m, 0)\rangle$, is straightforwardly derived as

$$\frac{\partial}{\partial t} C(n,t;m) = \mathcal{L}_C(n) C(n,t;m) \tag{32}$$

with

$$\mathcal{L}_C(n) = \left[\frac{\partial}{\partial \Delta t} \langle \mathcal{L}^*(n;\Delta t) \rangle \right]_{\Delta t \to 0} \tag{33}$$

Thus, the eigenvalues and eigenfunctions for $C(n,t;m)$ introduced in eq 23, $1/\tau_p$ and $f_p(n)$, are related to this operator $\mathcal{L}_C(n)$ as

$$\mathcal{L}_C(n) f_p(n) = -\frac{1}{\tau_p} f_p(n) \tag{34}$$

The eigenfunctions satisfy the boundary condition representing the instantaneous relaxation of the chain ends, $f_p(0) = f_p(N) = 0$, as well as the orthogonality relationship,

$$\frac{2}{N} \sum_{p=1}^{N} f_p(n) f_p(m) = \delta_{nm} \tag{35}$$

Eq 35 guarantees the Gaussian feature of the chain, $C(n,0;m) = \delta_{nm}$.

For a cross correlation function $S_2(n,m,t) = a^{-2} \langle u_x(n,t) u_y(m,t) \rangle$ representing an isochronal, shear orientational correlation of n-th and m-th subchains, the time evolution equation is similarly derived as[28]

$$\frac{\partial}{\partial t} S_2(n,m,t) = \mathcal{L}_S(n,m) S_2(n,m,t) \tag{36}$$

with

$$\mathcal{L}_S(n,m) = \left[\frac{\partial}{\partial \Delta t} \langle \mathcal{L}^*(n;\Delta t) \mathcal{L}^*(m;\Delta t) \rangle \right]_{\Delta t \to 0} \tag{37}$$

S_2 also satisfies the boundary condition representing the instantaneous relaxation at the chain ends,

$$S_2(n,m,t) = 0 \text{ for } n = 0, N \text{ and } m = 0, N \tag{38}$$

The shear orientation function describing the viscoelastic relaxation, $S(n,t) = a^{-2} \langle u_x(n,t) u_y(n,t) \rangle$ (*cf.* eq 2), is related to S_2 as $S(n,t) = S_2(n,n,t)$. For the chain and its constituent subchains being deformed uniformly under a small step shear strain γ at time 0, the initial conditions of S_2 and S are written as

$$S_2(n,m,0) = S_0 \delta_{nm}, \quad S(n,0) = S_0 \tag{39}$$

where the constant S_0 represents the initial orientational anisotropy of the subchains; $S_0 = \gamma/3$ for the affine deformation while $S_0 = 4\gamma/15$ (Doi-Edwards condition) for the affine deformation followed by equilibration of the subchain tension.[7]

As noted from eq 37, the operator $\mathcal{L}_S(n,m)$ for S_2 is affected by the short-time correlation of the motion of n-th and m-th subchains incorporated in the average $\langle \mathcal{L}^*(n;\Delta t) \mathcal{L}^*(m;\Delta t) \rangle$. In contrast, this correlation does not affect the operator $\mathcal{L}_C(n)$ for C, as noted in eq 33. Thus, in general, there is no unique relationship between $S_2(n,m,t)$ and $C(n,t;m)$ and thus between the viscoelastic and dielectric properties of type-A chains determined by $S_2(n,n,t)$ and $C(n,t;m)$. However, we can find

specific relationships for some extreme cases, as explained below.[28,30,33]

In an extreme case for which subchains in each chain exhibit completely *incoherent* (uncorrelated) motion in a short period of time, the operator in eq 37 is decoupled as $\langle \mathcal{L}^*(n;\Delta t) \mathcal{L}^*(m;\Delta t) \rangle = \langle \mathcal{L}^*(n;\Delta t) \rangle \langle \mathcal{L}^*(m;\Delta t) \rangle + O(\Delta t^2)$. (This incoherent subchain motion is incorporated in several kinds of dynamics, for example, the Rouse dynamics.) For this case, $\mathcal{L}_S(n,m)$ is equal to a sum $\mathcal{L}_C(n) + \mathcal{L}_C(m)$. Then, for the chain under the step strain, we can solve eq 36 under the boundary and initial conditions, eqs 38 and 39, to explicitly express $S_2(n,m,t)$ in terms of the eigenvalues and eigenfunctions defined for $C(n,t;m)$, $1/\tau_p$ and $f_p(n)$. For the orientation function, $S(n,t) = S_2(n,n,t)$, the result is summarized as[28,33]

$$S(n,t) = S_0 \frac{2}{N} \sum_{p=1}^{N} \{f_p(n)\}^2 \exp\left(-\frac{2t}{\tau_p}\right) \tag{40}$$

We can explicitly solve eq 36 also for other extreme case for which the subchain motion is completely *coherent* in each chain to satisfy a relationship $[\langle \mathcal{L}^*(n;\Delta t) \mathcal{L}^*(m;\Delta t) \rangle S_2(n,m,t)]_{n=m} = \langle \mathcal{L}^*(n;\Delta t) \rangle S_2(n,n,t) + O(\Delta t^2)$. (The coherent subchain motion is incorporated in several kinds of dynamics, for example, the reptation dynamics.) For this case, $S(n,t)$ is obtained as[28,33]

$$S(n,t) = 2S_0 \sum_{p=1}^{N} \left\{ \int_0^1 f_p(m) d(m/N) \right\} f_p(n) \exp\left(-\frac{t}{\tau_p}\right) \tag{41}$$

In both of eqs 40 and 41, the initial condition, $S(n,0) = S_0$, is guaranteed by the orthogonality relationship, eq 35.

As can be clearly noted from eqs 40 an 41, the dynamic viscoelastic modulus determined by $S(n,t)$ (*cf.* eq 2) exhibit different ω dependence for the cases of the incoherent and coherent subchain motion. This difference enables us to test the coherence of subchain motion in actual chains by comparing the modulus data with that calculated from $S(n,t)$ being expressed in terms of the dielectrically obtained $f_p(n)$ and τ_p. This comparison has been made,[28,30,33] and the results are summarized below.

The orientation functions $S(n,t)$ given by eqs 40 and 41 are integrated (summed) with respect to n to give the relaxation modulus $G(t)$ for the two cases of the incoherent and coherent subchain motion; *cf.* eq 2. Fourier transformation of this $G(t)$ gives the complex modulus $G^*(\omega) = G'(\omega) + iG''(\omega)$ with $i = \sqrt{-1}$. The results of this transformation can be conveniently expressed for the reduced modulus, $G_r^*(\omega) = \{M/cRT\}G^*(\omega)$ with M and c being the molecular weight and concentration of the chain, R being the gas constant, and T being the absolute temperature, as[28,33]

$$G_{r,inc}^*(\omega) = 2g \sum_{p=1}^{N} \left\{ \int_0^1 [f_p(n)]^2 d(n/N) \right\} \frac{i\omega\tau_p/2}{1 + i\omega\tau_p/2}$$
$$\text{for incoherent case} \tag{42}$$

$$G_{r,coh}^*(\omega) = 2Ng \sum_{p=1}^{N} \left\{ \int_0^1 f_p(n) d(n/N) \right\}^2 \frac{i\omega\tau_p}{1 + i\omega\tau_p}$$
$$\text{for coherent case} \tag{43}$$

Here, g is a factor determined by the choice of the initial condition for $S(n,t)$; $g = 1$ and $4/5$ for the affine condition ($S_0 = \gamma/3$) and the Doi-Edwards (DE) condition considering the equilibration of subchain tension ($S_0 = 4\gamma/15$). The affine and DE conditions are usually applied to non-entangled and entangled chains, respectively, but the difference between these conditions hardly affects the results of comparison shown below. It should be also noted that the integrals appearing in eqs 42 and 43 are independent of our choice of N (choice of the subchain size), but $G_{r,coh}^{*}$ straightforwardly changes with this choice because of the front factor N appearing in eq 43. In the comparison shown below, the entanglement segment is naturally chosen as the subchain for the entangled chain (i.e., $N = M/M_e$ for the entangled chain).

For the PI sample ($M = 48.8 \times 10^3$) in the solutions examined in Figure 11, the eigenvalues $1/\tau_p$ and the integrated/shifted eigenfunctions ΔF_p (Figure 10) for $p = 1$–3 have been determined dielectrically, as explained in the previous section. The $1/\tau_p$ and $f_p(n)$ data, the latter being obtained from numerical differentiation of the ΔF_p data, were utilized in eqs 42 and 43 to calculate the reduced moduli $G_{r,inc}^{*}$ and $G_{r,coh}^{*}$ for the cases of the incoherent and coherent subchain motion.[30] In Figure 12, these calculated moduli (curves) are compared with the G_r^{*} data of the PI sample (circles) obtained after subtraction of the G^{*} data of the solvent from the solution data. The plots for different PI concentrations ($c/c^{*} = 0.8$–27.1) are shifted vertically to avoid heavy overlapping of the data points. The PI chains with $c/c^{*} \leq 4.0$ ($c \leq 0.135 \, \text{g cm}^{-3}$) are in the non-entangled state, while those with $c/c^{*} \geq 8.0$ ($c \geq 0.272 \, \text{g cm}^{-3}$) are entangled with each other.

Since $G_{r,inc}^{*}$ and $G_{r,coh}^{*}$ were calculated from $1/\tau_p$ and $f_p(n)$ only for the lowest three eigenmodes, these moduli can be meaningfully compared with the data only at low ω where these eigenmodes dominantly contribute to the moduli. Thus, the real part of these moduli (storage moduli), $G'_{r,inc}$ and $G'_{r,coh}$, are shown with the solid curves in Figure 12 only at $\omega < 6/\tau_{1;G}$ ($\tau_{1;G}$ = the longest viscoelastic relaxation time) where this dominance of the lowest three eigenmodes was confirmed for the storage moduli.[30] The imaginary part (loss modulus) is shown only in the terminal flow regime at $\omega \ll 1/\tau_{1;G}$ because an approximate dominance of these eigenmodes was found only at those ω. Despite this limited aspect of the comparison, we note that the G_r^{*} data for the PI chain with $c/c^{*} \leq 4$ (in the non-entangled sate) are remarkably close to $G_{r,inc}^{*}$ (solid curves) for the case of incoherent subchain motion calculated with the affine condition, $g = 1$ in eq 42. The $G_{r,inc}^{*}$ at low ω shown here is independent of our choice of N, because the integral appearing in eq 42 is independent of N and $G_{r,inc}^{*}$ at those ω is dominated by the lowest three eigenmodes. Thus, the agreement between $G_{r,inc}^{*}$ and the G_r^{*} data unequivocally indicates that the non-entangled chain exhibits incoherent motion of its subchains. (No agreement between $G_{r,coh}^{*}$ and the G_r^{*} data was found for any choice of N, although the $G_{r,coh}^{*}$ curves are not shown for $c/c^{*} \leq 4$.)

Figure 12 also indicates that the G_r^{*} data deviate from $G_{r,inc}^{*}$ (solid curves) with increasing $c/c^{*} \geq 8.0$ (in the
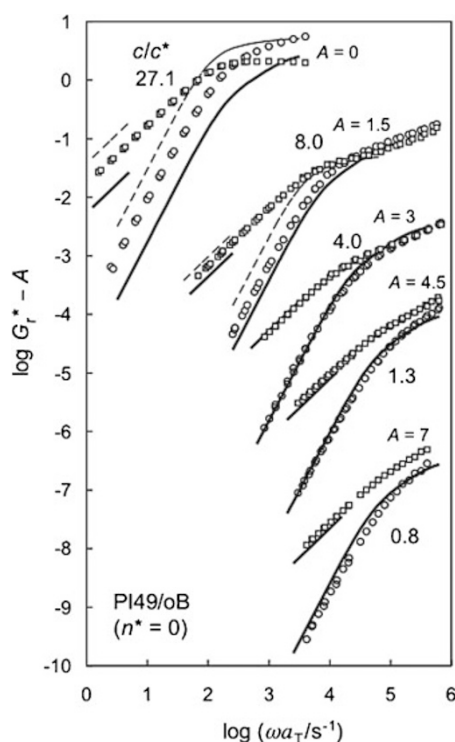

Figure 12. Reduced moduli G_r^{*} measured for linear PI ($M = 48.8 \times 10^3$) in the solutions examined in Figure 11. Solid and dotted curves indicate the reduced moduli $G_{r,inc}^{*}$ and $G_{r,coh}^{*}$ for the cases of the incoherent and coherent subchain motion evaluated from dielectrically determined eigenfunctions and eigenvalues.[30] The plots for different PI concentrations ($c/c^{*} = 0.8$–27.1) are shifted vertically to avoid heavy overlapping of the data points. The data taken from ref 30 with permission.

entangled regime). This result suggests that the entanglement provides the chain with some coherence of the subchain motion. However, the G_r^{*} data for $c/c^{*} \geq 8.0$ agree with neither $G_{r,inc}^{*}$ nor $G_{r,coh}^{*}$, the latter calculated with the DE condition, $g = 4/5$ in eq 43. ($G_{r,coh}^{*}$ calculated with $g = 1$ deviates from the G_r^{*} data more significantly.) Thus, no perfect coherence of the subchain motion is achieved for the entangled PI chain examined here. This lack of perfect coherence can be partly related to a contribution of the constraint release (CR) mechanism to the relaxation of this PI chain: The CR mechanism weakens the coherence, as noted from close coincidence of $G_{r,inc}^{*}$ and the G_r^{*} data of a probe PI chain relaxing through this mechanism in a short entangling matrix.[33] The G_r^{*} data of the same probe PI in a long entangling matrix (where the CR mechanism is suppressed) were found to agree with $G_{r,coh}^{*}$ for the case of coherent subchain motion,[33] which is in harmony with the incoherent feature of the CR mechanism.

In Figure 12, we also note a change of the ω dependence of the G_r^{*} data due to an increase of c in the non-entangled regime ($c \leq 4c^{*}$), from the Zimm-like dependence (at $c = 0.8c^{*}$) characterized by G'_r and G''_r not agreeing with each other in magnitude but commonly exhibiting a power-law type increase with ω to the Rouse-like dependence (at $c = 4c^{*}$) characterized by G'_r and G''_r agreeing with each other and exhibiting a power-

law type increase. In fact, the Zimm and Rouse models considerably well describe the G_r^* data for $c = 0.8c^*$ and $4c^*$, respectively. This result superficially supports a conventional molecular argument[1] that the screening of the hydrodynamic interaction with increasing c results in the Zimm-to-Rouse transition of the viscoelastic data. However, we should note that the Zimm-to-Rouse transition occurs just due to a change in the τ_p spacing and is not associated with a change in the functional form of the eigenfunction.[70] This is not the case for actual PI chain, as evidenced from the change of the eigenfunctions on the increase of c up to $4c^*$; see Figure 10. Thus, the change of the ω dependence of the G_r^* data with c in the non-entangled regime would be considerably contributed from a change of the inter-chain topological interaction discussed in the previous section, in addition to the screening of the hydrodynamic interaction that results in the simple Zimm-to-Rouse transition. This problem deserves further theoretical study.

NON-LINEAR DYNAMICS UNDER FAST SHEAR FLOW

Nonlinear viscoelastic features such as the nonlinear damping under large step strains and the shear thinning under fast flow are characteristics of entangled polymer chains.[1,7,9,10] As an example, Figure 13 shows the steady state shear viscosity $\eta(\dot{\gamma})$ and first normal stress difference coefficient $\Psi_1(\dot{\gamma})$ measured for a 15 wt% solution of a linear PI sample ($M = 1190 \times 10^3$) at 30 °C and a 20 wt% solution of a 6-arm star PI sample ($M_{arm} = 179 \times 10^3$) at 25 °C.[39] The solvent was an oligomeric butadiene ($M = 2 \times 10^3$). The linear PI sample has ~20 entanglements per chain in the solution, and the star PI sample has ~9 entanglements per span length (of the molecular weight $2M_{arm}$). The arrows indicate the terminal viscoelastic relaxation frequency at equilibrium, $1/\langle \tau_G \rangle$. The horizontal thick lines indicate the zero-shear viscosity η_0 and the zero-shear coefficient $\Psi_1(0)$ evaluated from linear viscoelastic G' and G'' data of the solutions;[39] $\eta_0 = [G''/\omega]_{\omega \to 0}$ and $\Psi_1(0) = [2G'/\omega G'']_{\omega \to 0} = 2\eta_0 J_e^o$ (J_e^o = steady state compliance). The $\eta(\dot{\gamma})$ and $\Psi_1(\dot{\gamma})$ data decrease significantly with $\dot{\gamma}$, and this shear-thinning behavior is characterized by power-law relationships,

$$\eta \propto \dot{\gamma}^{-\beta} \text{ and } \Psi_1 \propto \dot{\gamma}^{-\beta'} \text{ with } \beta \cong 0.8 \text{ and } \beta' \cong 1.6 \tag{44}$$
$$\text{for } \dot{\gamma} \gg 1/\langle \tau_G \rangle$$

Similar behavior has been reported for a variety of entangled sysems.[1,71–74]

The thinning behavior reflects strong orientation of the entangled chains under fast shear; cf. eq 1. In the fixed tube model explained in the earlier section, the chains are not stretched but almost fully oriented at $\dot{\gamma}$ well above $1/\langle \tau_G \rangle$ but below the Rouse frequency (which is the case for the data shown in Figure 13). For linear chains, the strong shear-orientation deduced from this model leads to very strong thinning, $\eta \propto \dot{\gamma}^{-1.5}$ for $\dot{\gamma} \gg 1/\langle \tau_G \rangle$ (cf. dotted curve in Figure 13), which corresponds to a physically unreasonable
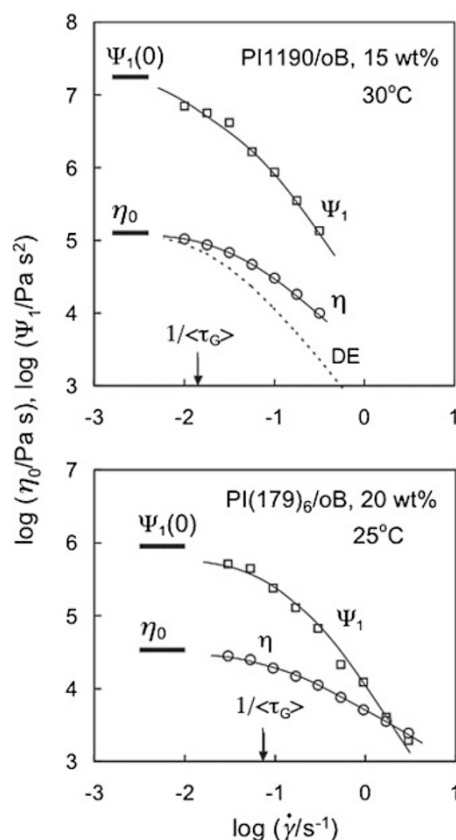

Figure 13. Steady state shear viscosity $\eta(\dot{\gamma})$ and first normal stress difference coefficient $\Psi_1(\dot{\gamma})$ measured for a 15 wt% solution of a linear PI sample ($M = 1190 \times 10^3$) at 30 °C and a 20 wt% solution of a 6-arm star PI sample ($M_{arm} = 179 \times 10^3$) at 25 °C.[39] The solvent was an oligomeric butadiene ($M = 2 \times 10^3$). The horizontal thick solid lines indicate the zero-shear viscosity η_0 and zero-shear coefficient $\Psi_1(0)$ obtained from linear viscoelastic (dynamic) measurements. The arrows denote the terminal relaxation frequency in the linear viscoelastic regime, $1/\langle \tau_G \rangle$. The data taken from ref 39 with permission.

decrease of the shear stress σ with $\dot{\gamma}$ ($\sigma \propto \dot{\gamma}^{-0.5}$).[7–10] Thus, the tube model has been refined by introducing a mechanism that moderately reduces the orientation under fast shear. Ianniruberto and Marrucci[75] considered a constraint release process for a given chain activated by convection (flow-induced motion) of surrounding/entangling chains. The Mead-Larson-Doi (MLD) model combines this convective constraint release (CCR) mechanism with the reptation and CLF mechanisms to excellently describe the η and Ψ_1 data in the thinning regime.[76] However, this combination results in a decrease of the relaxation time of the chains under fast shear, which is not consistent with recent experiments explained below.

For the PI/oB solutions examined in Figure 13, the dielectric data have been measured under steady shear.[39] The results are shown in Figure 14. In Figure 15, the terminal dielectric relaxation time $\langle \tau_\varepsilon \rangle$ and dielectric intensity $\Delta\varepsilon$ evaluated from those data are plotted against the normalized shear rate, $\dot{\gamma}\langle \tau_G \rangle$. (The measurements were successfully made with electrodes mounted on a rheometer:[39] One electrode had a blade immersed in a mercury reservoir connected to a dielectric
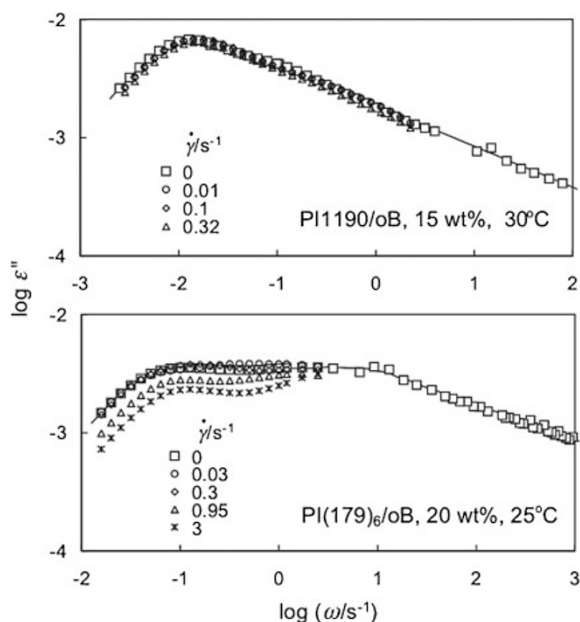
Figure 14. Dielectric data measured for a 15 wt % solution of a linear PI sample ($M = 1190 \times 10^3$) at 30 °C and a 20 wt % solution of a 6-arm star PI sample ($M_{arm} = 179 \times 10^3$) at 25 °C under steady shear at the rates as indicated.[39] The data taken from ref 39 with permission.
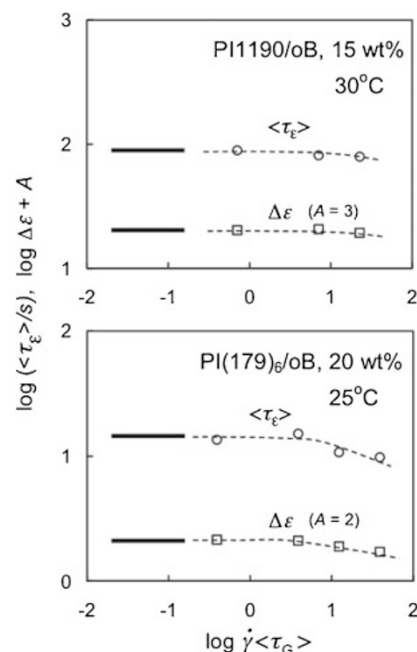

Figure 15. Terminal dielectric relaxation time $\langle \tau_\varepsilon \rangle$ and dielectric intensity $\Delta\varepsilon$ under steady shear obtained for the PI solutions examined in Figures 13 and 14.[39] The $\langle \tau_\varepsilon \rangle$ and $\Delta\varepsilon$ data are plotted against the normalized shear rate, $\dot{\gamma}\langle \tau_G \rangle$. The data taken from ref 39 with permission.

bridge so that the rotation of this electrode did not disturb the measurement.)

For the star PI chains (having the type-A dipoles diverging from the branching point), $\langle \tau_\varepsilon \rangle$ and $\Delta\varepsilon$ decrease moderately and the dielectric mode distribution broadens a little with increasing $\dot{\gamma}$ up to $3\,s^{-1} \cong 40/\langle \tau_G \rangle$; see bottom panels of Figures 14 and 15. These changes are much less significant, in magnitude, compared to the very strong decreases of the viscoelastic η and Ψ_1 data; *cf.* bottom panel of Figure 13. For the linear PI chains (having non-inverted type-A dipoles), the shear effect is even smaller: As seen in the top panels of Figures 14 and 15, the dielectric behavior of linear PI is practically unaffected by the fast shear in the range of $\dot{\gamma} \leq 30/\langle \tau_G \rangle$, despite the significant nonlinearity seen for the viscoelastic data (Figure 13). The dielectric behavior of linear PI was also examined under large-amplitude oscillatory strain (LAOS) at an angular frequency $> 1/\langle \tau_G \rangle$, and a very minor shear effect on the dielectric data (comparable to that seen in Figures 14 and 15) was observed together with a significant viscoelastic nonlinearity.[46,47]

The molecular expression of the dielectric relaxation function, eq 5, is rigorously derived only at equilibrium where the Green-Kubo theorem is valid.[77–79] However, for linear PI, a recent analysis based on the Langevin equation and non-equilibrium statistical calculation indicates that the characteristic times $\tau_{p;\varepsilon}$ of the dielectric relaxation modes under steady shear are exactly the same as those of the end-to-end vector fluctuation modes defined in the shear gradient direction and the dielectric mode distribution agrees with the fluctuation mode distribution at least up to terms of the second order of

$\dot{\gamma}$.[79] Namely, the normalized dielectric relaxation function and dielectric intensity of linear PI under *steady shear* are satisfactorily expressed as $\Phi(t) = \langle R_y(t)R_y(0)\rangle_{ss}/\langle R_y^2\rangle_{ss}$ and $\Delta\varepsilon = K\nu\langle R_y^2\rangle_{ss}$, respectively, where $R_y(t)$ is the component of the end-to-end vector in the y direction ($=$ shear gradient direction), $\langle \cdots \rangle_{ss}$ indicates the average under steady shear, K is a proportionality constant determined by the magnitude of type-A dipole per unit length of the chain backbone, and ν is the number density of the chain. These expressions should also apply to star chains, given that the $R_y(t)$ term therein is replaced by a sum of the end-to-end vectors of the star arms. (Under LAOS, the conformational distribution function is coupled with LAOS and oscillates around a base part at LAOS frequency. The ε'' data of the chains under LAOS correspond to the above averages $\langle \cdots \rangle$ taken over this time-independent base part of the distribution function.[79])

Thus, the $\dot{\gamma}$-insensitivity of the dielectric data of the linear PI chains unequivocally indicates that the end-to-end vector fluctuation behavior of the chains in the shear gradient direction is insensitive to the shear. The refined tube model (MLD model),[76] that incorporates the CCR mechanism and describes the nonlinear viscoelastic data excellently, predicts that the relaxation time under steady shear decreases with increasing $\dot{\gamma}$ because the entanglement number per chain decreases with $\dot{\gamma}$ through the CCR mechanism. Thus, this model does not appear to describe the viscoelastic and dielectric data consistently.

In the molecular simulation referred to as NAPLES simulation, the entanglements are represented as slip-links and the chain motion and slip-link motion are simultaneously

calculated according to the microscopic forces acting on the chains/slip-links.[80] This simulation predicts the experimentally unobserved decrease of the relaxation time under fast shear,[79,81] despite its excellent description of the viscoelastic data.[80,82] As for the NAPLES simulation, it was also found that incorporation of a mechanism of hidden entanglement appearance (HEA)[83] improves the description for the dielectric data while keeping the accuracy of description for the viscoelastic data.[79,81] In this HEA mechanism, a chain in a vicinity of a given chain (probe) but not entangled with the probe before occurrence of the CCR jump provides a topological constraint for the probe after this jump. This constraint occurs isotropically in space and thus hardly affects the viscoelastic stress, but it still retards the chain motion thereby tending to suppress the acceleration of the relaxation due to CCR. This result suggests that the dynamics of entanglement reformation is the key in the consistent description of the dielectric and viscoelastic properties under fast shear. This reformation dynamics does not seem to be properly incorporated in the widely utilized molecular models. A further study is desired for this issue.

Finally, a comment needs to be made for the uniformity of fast shear flow. For highly entangled polymers having $M/M_e > 50$ (not for the moderately entangled materials such as the solutions examined in Figures 13–15), Wang *et al.* reported that the steady flow behavior under controlled stress in the nonlinear regime does not necessary agree with the flow behavior under controlled strain rate and that the shear field is not uniform for both cases.[84–86] This non-uniformity of flow is somewhat similar to the shear-banding seen in textured fluids.[87,88]

Even under large stress/high strain rate, the polymer chains should exhibit linear viscoelastic behavior at short time where the strain remains smaller than a critical value (~ 1). However, the chain conformation under the conditions of controlled stress and controlled strain rate should be different even in this short time regime (as explained in the next section), and this difference could have been amplified at long times to give a difference of the nonlinear steady flow behavior under these conditions. A mechanism of achieving the non-uniform shear field for highly entangled chains could be also related to this conformational difference. This mechanism might be related to local disentanglement (rupture of entanglement mesh) discussed by Wang *et al.*[84,85] However, details of this mechanism have not been elucidated, and a further study is strongly desired.

CREEP BEHAVIOR OF BEAD-SPRING CHAIN

In relation to the flow non-uniformity explained in the previous section, it is important and interesting to analyze the conformation of polymer chains in the transient state under the conditions of controlled stress and controlled strain rate. However, in earlier work, the analysis was never made under the condition of controlled stress: Surprisingly, no analysis was made even for the bead-spring chain (Rouse chain), the fundamental model chain for non-entangled polymers being

also utilized as the central object in all models for entangled polymers.[7–10] For this problem, the analysis under constant stress was recently made for the bead-spring chains of various architectures.[89–92] The results are summarized below.

We consider a linear Rouse chain composed of N beads connected by Gaussian springs of the strength κ. Each bead has a friction coefficient ζ. The bead and spring, respectively, represent the friction and elasticity of the Rouse segment utilized as the subchain in the model. The Langevin equation describing the time evolution of the position $\mathbf{r}(n,t)$ of n-th bead under a simple shear field can be written, in the continuous limit, as[7,9,89]

$$\zeta\left\{\frac{\partial}{\partial t}\mathbf{r}(n,t) - \mathbf{V}(n,t)\right\} = \kappa\frac{\partial^2}{\partial n^2}\mathbf{r}(n,t) + \mathbf{F}_B(n,t)$$
$$\text{for } 0 < n < N \tag{45}$$

where $\mathbf{F}_B(n,t)$ is the random thermal force acting on n-th segment at time t: $\mathbf{F}_B(n,t)$ is modeled as a white noise being characterized, in the continuous limit, by relationships, $\langle\mathbf{F}_B(n,t)\rangle = \mathbf{0}$ and $\langle\mathbf{F}_B(n,t)\mathbf{F}_B(n',t')\rangle = 2\mathbf{I}\zeta k_B T\delta(n-n')\delta(t-t')$ with $\mathbf{I}$ = unit tensor. $\mathbf{V}(n,t)$ represents a velocity of a frictional medium for the bead. For a simple, uniform shear flow at a rate $\dot{\gamma}(t)$, $\mathbf{V}(n,t)$ is given by

$$\mathbf{V}(n,t) = \dot{\gamma}(t)\begin{bmatrix} r_y(n,t) \\ 0 \\ 0 \end{bmatrix} \tag{46}$$

where the shear and shear-gradient directions are chosen to be x and y directions, and r_y is the y component of $\mathbf{r}$. The bond vector for the Rouse segment (subchain) is given by $\mathbf{u}(n,t) = \partial\mathbf{r}(n,t)/\partial n$, and the spring constant κ is related to mean-square segment size at equilibrium, $\kappa = 3k_B T/a^2$ with $a^2 = \langle\mathbf{u}^2\rangle_{\text{eq}}$. The boundary condition representing the lack of external force acting on the chain ends is given by

$$\mathbf{u}(n,t) = \mathbf{0} \quad \text{for } n = 0, N \tag{47}$$

In the continuous limit, the shear stress $\sigma(t)$ of an ensemble of the Rouse chains (with the number density ν) is related to chain conformation as (*cf.* eq 1)

$$\sigma(t) = 3\nu k_B T\int_0^N S(n,t)\mathrm{d}n$$
$$\text{with} \quad S(n,t) = \frac{1}{a^2}\langle u_x(n,t)u_y(n,t)\rangle \tag{48}$$

Thus, $S(n,t)$ can be formally calculated from eqs 45–48 under either the condition of controlled strain rate ($\dot{\gamma}(t) =$ known) or the condition of controlled stress ($\sigma(t) =$ known) as[92]

$$S(n,t) = \frac{2\sigma_{\text{ss}}}{\nu N k_B T}\sum_{p\geq 1}A_p(t)\sin^2\left(\frac{p\pi n}{N}\right) \tag{49}$$

Here, $A_p(t)$ is a normalized orientational anisotropy defined for p-th Rouse eigenmodes, $A_p(t) \equiv \{\nu k_B T p^2\pi^2/2\sigma_{\text{ss}}Na^2\}\langle X_p(t)Y_p(t)\rangle$ with $X_p(t)$ and $Y_p(t)$ being the x and y components of the Rouse eigenvector $(2/N)\int_0^N\mathbf{r}(n,t)\cos(p\pi n/N)\mathrm{d}n$, and σ_{ss} represents the shear stress in the steady state; σ_{ss}

is expressed in terms of the shear rate $\dot{\gamma}_{ss}$ in this state and the longest viscoelastic Rouse relaxation time τ_R as[92]

$$\sigma_{ss} = \frac{\pi^2}{6} \nu k_B T \tau_R \dot{\gamma}_{ss} \quad \text{(with } \tau_R = \zeta N^2 a^2 / 6\pi^2 k_B T) \quad (50)$$

Under the condition of controlled strain rate, all Rouse eigenmodes are independent to each other and their anisotropies $A_p(t)$ can be straightforwardly calculated from eqs 45–47. For example, $A_p(t)$ after start-up of shear at constant $\dot{\gamma}$ ($= \dot{\gamma}_{ss}$) at time 0 is obtained as[89,90]

$$A_p(t) = \frac{2}{p^2\pi^2}\left\{1 - \exp\left(-\frac{p^2 t}{\tau_R}\right)\right\} \quad (51)$$

under constant rate flow at $t > 0$

In contrast, under the condition of controlled stress, we need to couple eqs 45 and 48 to calculate $A_p(t)$. These coupled equations can be still solved analytically with the Laplace transformation method to calculate $A_p(t)$. For example, for the creep process under a constant stress σ ($= \sigma_{ss}$) at $t > 0$, $A_p(t)$ is obtained as[89,90]

$$A_p(t) = \frac{2}{p^2\pi^2} + \frac{4}{3\pi^2}\sum_{q\geq 1}\frac{1}{p^2 - (\theta_q/\pi)^2}\exp\left(-\frac{\theta_q^2 t}{\pi^2 \tau_R}\right) \quad (52)$$

during creep process

Here, θ_q is a numerical factor determined by

$$\theta_q = \tan\theta_q \quad \text{(with } q\pi < \theta_q < q\pi + \pi/2) \quad (53)$$

As a byproduct of the calculation of $A_p(t)$, the recoverable part of the creep compliance of the Rouse chain, $J_r(t)$, is analytically obtained as

$$J_r(t) = \frac{4}{\nu k_B T}\sum_{p\geq 1}\frac{1}{\theta_p^2}\left\{1 - \exp\left(-\frac{\theta_p^2 t}{\pi^2 \tau_R}\right)\right\} \quad (54)$$

(Surprisingly, this analytical expression of $J_r(t)$ was obtained only recently,[89] despite the extensive use of the Rouse model for five decades.)

As seen from eqs 51 and 52, the anisotropy A_p of the Rouse mode in the steady state (at $t = \infty$) is the same under the conditions of controlled strain rate and stress, which leads to coincidence of the steady state orientation function S_{ss} (eq 49) under these conditions. This coincidence of S_{ss} is a general consequence of the linear response of polymer chains. However, before the steady state is achieved, $S(n, t)$ is quite different under the two conditions. This difference is demonstrated in Figure 16 where a normalized orientation function, $\tilde{S}(n, t) = \{\nu N k_B T / \sigma_{ss}\}S(n, t)$ at several representative t, is plotted against a normalized segment index n/N.[89,90] After start-up of constant rate flow (top panel of Figure 16), the orientational anisotropy *monotonically* grows toward the steady state value. This growth is slower at $n/N = 1/2$ (chain center) than at $n/N \cong 0, 1$ (chain ends), because the chain center is less mobile (contributed more from the slow eigenmodes) compared to the chain ends. In contrast, during the creep process under a constant stress (bottom panel), the anisotropy at around the chain ends does not grow monotonically but exhibits overshoot before it approaches the steady state value. This
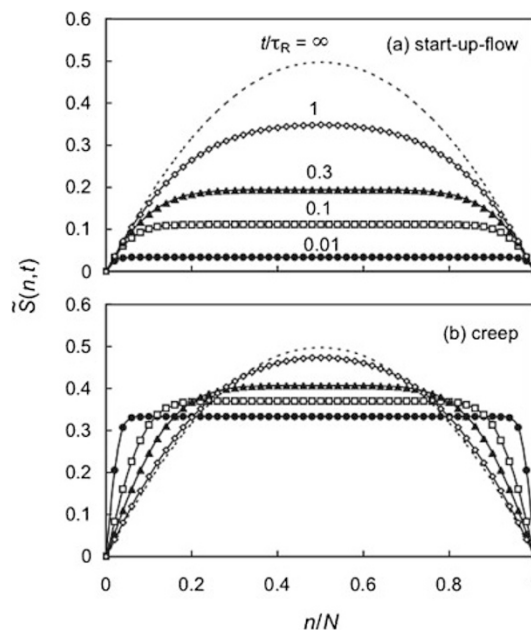

Figure 16. Time evolution of normalized orientation function $\tilde{S}(n, t)$ calculated for a linear bead-spring chain (Rouse chain) after start-up of constant rate flow (top panel) and during creep under constant stress (bottom panel). $\tilde{S}(n, t)$ is plotted against a normalized segment index n/N. The data taken from ref 90 with permission.

overshoot is a natural consequence of the constant stress condition: The integral of $S(n, t)$ is required to be constant under this condition (*cf.* eq 48) so that the mobile chain ends are forced to exhibit the overshoot, at short t, thereby compensating the slow growth of anisotropy at the less mobile chain center. The corresponding compensation through undershoot of $S(n, t)$ at $n/N \cong 0, 1$ is noted during the creep recovery process after removal of the stress.[89,90] (The compensation is achieved through the coupling of the Rouse eigenmodes.)

The chain conformation including the orientational anisotropy has been analyzed also for star-branched[91] and ring-shaped[92] bead-spring chains, the former being often referred to as the Rouse-Ham chain. For both of the star and ring chains, the conformational difference was found in the transient state under the conditions of the constant strain rate and constant stress, as similar to the behavior of the linear chain. Furthermore, the orientational anisotropy of the star chain under steady shear was found to be concentrated at the branching point more significantly compared to the middle point of the linear chain, and the corresponding analytical expression of the creep compliance was also obtained.[91] For the ring chain during the creep process under constant stress, the orientational anisotropy is the same throughout the chain backbone (because all segments of this chain are equivalent to each other) and *independent of t*, but the strain growth exhibits retardation.[92] (This retardation of the strain growth is essentially the same as that for the linear chain and described by eq 54 with the factors $4/\nu k_B T$ and τ_R therein being replaced by $2/\nu k_B T$ and $\tau_{ring} = \zeta N^2 a^2 / 24\pi^2 k_B T$.[92]) A detailed analysis revealed that the retardation of the strain growth of the ring

chain reflects a retarded growth of orientational cross corre-lation of arbitrary two segments in the chain backbone.[92] (For the linear and star chains, the retarded strain growth is contributed from this retardation of the cross-correlation growth in addition to the time evolution of the anisotropy of individual segments.)

Finally, a comment needs to be made in relation to the conformational difference of the bead-spring chain in the transient state under the conditions of constant strain rate and constant stress. This difference is not limited to the bead-spring chain but should emerge also for actual entangled chains. For the bead-spring chain, the shear flow is stable so that the difference in the transient state vanishes at long times and no nonlinearity prevails for the shear stress. However, for the entangled chains exhibiting a significant nonlinearity, the conformational difference in the transient state under the conditions of constant stress and constant strain rate *might* result in bifurcation of the chain conformation at long t, and this bifurcation *could* lead to the non-uniform shear fields explained in the previous section. It is an interesting subject of future work to examine a possibility of this bifurcation for the entangled chains.

CONCLUDING REMARKS

In this article, we have summarized some of recent findings for the global dynamics in homopolymer liquids. Comparison of viscoelastic and dielectric data of type-A chains suggests that the molecular picture of partial DTD (dynamic tube dilation), that coarse-grains the length and time scales self-consistently in accord to the constraint (CR) release dynamics, is valid for description of the entanglement dynamics. This validity is intimately related to the freedom in the choice of the *internally equilibrated* subchain for description of the physical properties. The dielectric data for dipole-inverted type-A chains allow us to experimentally determine the eigenfunctions and eigenvalues for the local correlation function (defined without coarse-graining). Occurrence of the intra-chain coher-ence of subchain motion due to the entanglement, deduced from comparison of the viscoelastic modulus data with the modulus calculated from these eigenfunctions and eigenvalues, is consistent with the partial DTD picture. The dielectric behavior of entangled type-A chains under fast shear flow indicates a flow-insensitivity of the end-to-end fluctuation dynamics in the shear-gradient direction. This insensitivity strongly suggests a necessity of refinement of current molecu-lar models through incorporation of a proper mechanism of entanglement reformation. Finally, conformational analysis of bead-spring chains under conditions of constant strain rate and constant stress reveals a difference of the orientational anisotropy in the transient flow state under these conditions. This difference might be relevant to non-uniformity of shear flow noted for highly entangled chains.

A comment needs to be made also for the dynamics of entangled ring chains with a high purity (very low contami-nation of linear prepolymers) that has been studied recently[93–95]

but is not explained in this article. Remarkable slowing and mode-narrowing have been found on addition of a small amount of linear polymers to the pure ring.[94] This effect of linear chains provides us with a clue for specifying the topological constraint (or entanglement) for the ring chains having no ends. Another interesting problem is the effect of spatial and thermodynamic confinement on the global dynam-ics (mode broadening).[23,26,96] These issues deserve further study from both of the experimental and theoretical aspects.

Apart from the details of the dynamic features of homopol-ymer liquids explained in this article, we note that the combination of dielectric and viscoelastic methods was essential for revealing these features. The usefulness of this combination has been noted also for a variety of multi-component systems containing PI.[68,96–104] For example, for miscible blends of PI with poly(*p-tert*-butyl styrene) having no type-A dipole, the PI dynamics was observed dielectrically thereby enabling us to examine the effect of dynamic heterogeneity on the global chain dynamics.[100–102] Another example is found for microphase-separated PS-PI-PS triblock copolymers composed of PI and polystyrene (PS) blocks. The PI block therein takes either the loop or bridge conformations. However, the bridge faction ϕ_b was not clearly estimated and the bridge elasticity was not well quantified in previous experiments. A challenge to this loop/bridge problem was made with the aid of the dielectric data measured for the copolymers having barely entangled PI blocks with once-inverted type-A dipoles.[96,97] Those data, detecting the fluctua-tion of the midpoint of the PI blocks, were found to be similar to the data of PS-PI diblock copolymers detecting the free end fluctuation of the tail-type PI blocks therein. A thermodynamic consideration for this similarity gave an estimate, $\phi_b \cong 0.4$ in bulk[97] and concentrated solutions in a PI-selective solvent (copolymer concentration $c = 50\,\text{wt}\,\%$),[96] which agrees well with the self-consistent field calculation.[105] On dilution of the copolymer to $c = 20\,\text{wt}\,\%$ (a little above the syneresis point), ϕ_b decreased to $\cong 0.2$ because of the stretching/destabilization of the bridge conformation. These results were combined with the viscoelastic data to reveal that the elasticity sustained per barely entangled bridge-type block is of the same order $(= O(k_B T))$ as the elasticity per tail-type block (being sustained through the osmotic interaction).[97] This result is complemen-tary to the result found for well entangled bridges, the elasticity per bridge much larger than $k_B T$ (as quantified by the use of a ring block copolymer as a reference for the loops).[106,107]

Thus, the combination of different methods of physical measurements, not only the viscoelastic and dielectric methods but also the dichroism, scattering, and NMR methods,[64–67] enables us to reveal novel features of flexible polymers. It is of particular scientific interest to explore the universality under-lying these features.

Polymer
Journal

REFERENCES

1. J. D. Ferry, "Viscoelastic Properties of Polymers," 3rd ed., Wiley, New York, 1980.
2. T. Inoue, H. Okamoto, and K. Osaki, *Macromolecules*, **24**, 5670 (1991).
3. K. Osaki, H. Okamoto, T. Inoue, and E. J. Hwang, *Macromolecules*, **28**, 3625 (1995).
4. T. Inoue and K. Osaki, *Macromolecules*, **29**, 1595 (1996).
5. T. Inoue, Y. Miyazaki, H. Okamoto, H. Matsui, H. Watanabe, T. Kanaya, and K. Osaki, *Macromolecules*, **29**, 6240 (1996).
6. K. Osaki and T. Inoue, *Macromolecules*, **29**, 7622 (1996).
7. M. Doi and S. F. Edwards, "The Theory of Polymer Dynamics," Clarendon, Oxford, 1986.
8. W. W. Graessley, *Adv. Polym. Sci.*, **47**, 67 (1982).
9. H. Watanabe, *Prog. Polym. Sci.*, **24**, 1253 (1999).
10. T. C. B. McLeish, *Adv. Phys.*, **51**, 1379 (2002).
11. R. Cole, *J. Chem. Phys.*, **42**, 637 (1965).
12. K. Adachi and T. Kotaka, *Prog. Polym. Sci.*, **18**, 585 (1993).
13. H. Watanabe, *Macromol. Rapid Commun.*, **22**, 127 (2001).
14. Y. Imanishi, K. Adachi, and T. Kotaka, *J. Chem. Phys.*, **89**, 7585 (1988).
15. H. Yoshida, K. Adachi, H. Watanabe, and T. Kotaka, *Polym. J.*, **21**, 863 (1989).
16. K. Adachi, S. Itoh, I. Nishi, and T. Kotaka, *Macromolecules*, **23**, 2554 (1990).
17. H. Yoshida, H. Watanabe, K. Adachi, and T. Kotaka, *Macromolecules*, **24**, 2981 (1991).
18. O. Urakawa, K. Adachi, and T. Kotaka, *Macromolecules*, **26**, 2036 (1993).
19. O. Urakawa, K. Adachi, and T. Kotaka, *Macromolecules*, **26**, 2042 (1993).
20. D. Boese, F. Kramer, and L. J. Fetters, *Makromol. Chem., Rapid Commun.*, **9**, 367 (1988).
21. D. Boese and F. Kramer, *Macromolecules*, **23**, 829 (1990).
22. D. Boese, F. Kramer, and L. J. Fetters, *Macromolecules*, **23**, 1826 (1990).
23. L. Petychakis, G. Floudas, and G. Fleischer, *Eur. Phys. Lett.*, **40**, 685 (1997).
24. G. Floudas and T. Reisinger, *J. Chem. Phys.*, **111**, 5201 (1999).
25. G. Floudas, C. Gravalides, T. Reisinger, and G. Wegner, *J. Chem. Phys.*, **111**, 9847 (1999).
26. Y. K. Cho, H. Watanabe, and S. Granick, *J. Chem. Phys.*, **110**, 9688 (1999).
27. H. Watanabe, O. Urakawa, and T. Kotaka, *Macromolecules*, **26**, 5073 (1993).
28. H. Watanabe, O. Urakawa, and T. Kotaka, *Macromolecules*, **27**, 3525 (1994).
29. H. Watanabe, H. Yamada, and O. Urakawa, *Macromolecules*, **28**, 6443 (1995).
30. H. Watanabe, M.-L. Yao, and K. Osaki, *Macromolecules*, **29**, 97 (1996).
31. O. Urakawa and H. Watanabe, *Macromolecules*, **30**, 652 (1997).
32. Y. Matsumiya, H. Watanabe, K. Osaki, and M.-L. Yao, *Macromolecules*, **31**, 7528 (1998).
33. H. Watanabe, Y. Matsumiya, K. Osaki, and M.-L. Yao, *Macromolecules*, **31**, 7538 (1998).
34. Y. Matsumiya, H. Watanabe, T. Inoue, K. Osaki, and M.-L. Yao, *Macromolecules*, **31**, 7973 (1998).
35. Y. Matsumiya, H. Watanabe, and K. Osaki, *Macromolecules*, **33**, 499 (2000).
36. H. Watanabe, Y. Matsumiya, and K. Osaki, *J. Polym. Sci., Part B: Polym. Phys.*, **38**, 1024 (2000).
37. Y. Matsumiya and H. Watanabe, *Macromolecules*, **34**, 5702 (2001).
38. H. Watanabe, Y. Matsumiya, and T. Inoue, *Macromolecules*, **35**, 2339 (2002).
39. H. Watanabe, S. Ishida, and Y. Matsumiya, *Macromolecules*, **35**, 8802 (2002).
40. H. Watanabe, S. Ishida, Y. Matsumiya, and T. Inoue, *Macromolecules*, **37**, 1937 (2004).
41. H. Watanabe, S. Ishida, Y. Matsumiya, and T. Inoue, *Macromolecules*, **37**, 6619 (2004).
42. H. Watanabe, T. Sawada, and Y. Matsumiya, *Macromolecules*, **39**, 2553 (2006).
43. X. Qiao, T. Sawada, Y. Matsumiya, and H. Watanabe, *Macromolecules*, **39**, 7333 (2006).
44. T. Sawada, X. Qiao, and H. Watanabe, *Nihon Reoroji Gakkaishi*, **35**, 11 (2007).
45. H. Watanabe, Y. Matsumiya, E. van Ruymbeke, D. Vlassopoulos, and N. Hadjichristidis, *Macromolecules*, **41**, 6110 (2008).
46. S. Höfl, F. Kremer, H. W. Spiess, M. Wilhelm, and S. Kahle, *Polymer*, **47**, 7282 (2006).
47. S. Capaccioli, D. Prevosto, A. Best, A. Hanewald, and T. Pakula, *J. Non-Cryst. Solids*, **353**, 4267 (2007).
48. M. Doi and S. F. Edwards, *J. Chem. Soc., Faraday Trans. 2*, **74**, 1789 (1978).
49. M. Doi and S. F. Edwards, *J. Chem. Soc., Faraday Trans. 2*, **74**, 1802 (1978).
50. M. Doi and S. F. Edwards, *J. Chem. Soc., Faraday Trans. 2*, **74**, 1818 (1978).
51. M. Doi, *J. Polym. Sci., Polym. Phys. Ed.*, **21**, 667 (1983).
52. D. S. Pearson and E. Helfand, *Macromolecules*, **17**, 888 (1984).
53. A. Likhtman and T. C. B. McLeish, *Macromolecules*, **35**, 6332 (2002).
54. R. S. Graham, A. E. Likhtman, and T. C. B. McLeish, *J. Rheol.*, **47**, 1171 (2003).
55. G. Marrucci, *J. Polym. Sci., Polym. Phys. Ed.*, **23**, 159 (1985).
56. R. C. Ball and T. C. B. McLeish, *Macromolecules*, **22**, 1911 (1989).
57. S. T. Milner and T. C. B. McLeish, *Macromolecules*, **30**, 2159 (1997).
58. S. T. Milner and T. C. B. McLeish, *Macromolecules*, **31**, 7479 (1998).
59. S. T. Milner and T. C. B. McLeish, *Phys. Rev. Lett.*, **81**, 725 (1998).
60. S. T. Milner, T. C. B. McLeish, R. N. Young, A. Hakiki, and J. M. Johnson, *Macromolecules*, **31**, 9345 (1998).
61. S. J. Park, S. Shanbhag, and R. G. Larson, *Rheol. Acta*, **44**, 319 (2005).
62. E. van Ruymbeke, K. Orfanou, M. Kapnistos, H. Iatrou, M. Pitsikalis, N. Hadjichristidis, D. J. Lohse, and D. Vlassopoulos, *Macromolecules*, **40**, 5941 (2007).
63. E. van Ruymbeke, R. Keunings, and C. Bailly, *J. Non-Newtonian Fluid Mech.*, **128**, 7 (2005).
64. W. J. Walczak and R. P. Wool, *Macromolecules*, **24**, 4657 (1991).
65. C. M. Ylitalo, G. G. Fuller, and D. S. Pearson, *Rheol. Acta*, **29**, 543 (1990).
66. J. A. Kornfield, G. G. Fuller, and D. S. Pearson, *Macromolecules*, **22**, 1334 (1989).
67. K. A. Welp, R. P. Wool, G. Agrawal, S. K. Satija, S. Pispas, and J. Mays, *Macromolecules*, **32**, 5127 (1999).
68. Y. Hirose, O. Urakawa, and K. Adachi, *J. Polym. Sci., Part B: Polym. Phys.*, **42**, 4084 (2004).
69. B. H. Zimm, *J. Chem. Phys.*, **24**, 269 (1956).
70. H. Yamakawa, "Modern Theory of Polymer Solutions," Harper & Row, New York, 1971.
71. W. W. Graessley, *Adv. Polym. Sci.*, **16**, 1 (1974).
72. K. Osaki, S. Kimura, and M. Kurata, *J. Polym. Sci., Polym. Phys. Ed.*, **19**, 517 (1981).
73. J. J. Magda, C. S. Lee, S. J. Muller, and R. G. Larson, *Macromolecules*, **26**, 1696 (1993).

949

74. E. F. Brown, W. R. Burghardt, H. Kahvand, and D. C. Venerus, *Rheol. Acta*, **34**, 221 (1995).
75. G. Ianniruberto and G. Marrucci, *J. Non-Newtonian Fluid Mech.*, **65**, 241 (1996).
76. D. W. Mead, R. G. Larson, and M. Doi, *Macromolecules*, **31**, 7895 (1998).
77. R. H. Cole, *J. Chem. Phys.*, **42**, 637 (1965).
78. E. Riande and E. Saiz, "Dipole Moments and Birefringence of Polymers," Prentice Hall, Englewood Cliffs, NJ, 1992.
79. T. Uneyama, Y. Masubuchi, K. Horio, Y. Matsumiya, H. Watanabe, J. A. Pathak, and C. M. Roland, *J. Polym. Sci., Part B: Polym. Phys.*, **47**, 1039 (2009).
80. Y. Masubuchi, J. Takimoto, K. Koyama, G. Ianniruberto, F. Greco, and G. Marrucci, *J. Chem. Phys.*, **115**, 4387 (2001).
81. Y. Masubuchi, H. Watanabe, G. Ianniruberto, F. Greco, and G. Marrucci, *Nihon Reoroji Gakkaishi*, **32**, 197 (2004).
82. Y. Masubuchi, G. Ianniruberto, F. Greco, and G. Marrucci, *J. Non-Newtonian Fluid Mech.*, **149**, 87 (2008).
83. G. Ianniruberto and G. Marrucci, *J. Non-Newtonian Fluid Mech.*, **95**, 363 (2000).
84. P. Tapadia and S. Q. Wang, *Macromolecules*, **37**, 9083 (2004).
85. P. Tapadia, S. Ravindranath, and S. Q. Wang, *Phys. Rev. Lett.*, **96**, 196001 (2006).
86. S. Q. Wang, S. Ravindranath, Y. Y. Wang, and P. Y. Boukany, *J. Chem. Phys.*, **127**, 064903 (2007).
87. M. R. López-González, W. M. Holmes, P. T. Callaghan, and P. J. Photinos, *Phys. Rev. Lett.*, **93**, 268302 (2004).
88. P. T. Mather, H. G. Jeon, C. D. Han, and S. Chang, *Macromolecules*, **33**, 7594 (2000).
89. H. Watanabe and T. Inoue, *Rheol. Acta*, **43**, 634 (2004).
90. H. Watanabe and T. Inoue, *J. Phys.: Condens. Matter*, **17**, R607 (2005).
91. Y. Matsumiya, T. Inoue, Y. Oishi, and H. Watanabe, *J. Polym. Sci., Part B: Polym. Phys.*, **44**, 3501 (2006).
92. H. Watanabe, T. Inoue, and Y. Matsumiya, *Macromolecules*, **39**, 5419 (2006).
93. M. Rubinstein, *Phys. Rev. Lett.*, **57**, 3023 (1986).
94. M. Kapnistos, M. Lang, D. Vlassopoulos, W. Pyckhout-Hintzen, D. Richter, D. Cho, T. Chang, and M. Rubinstein, *Nat. Mater.*, **7**, 997 (2008).
95. D. Kawaguchi, A. Takano, Y. Matsushita, K. Tanaka, T. Nagamura, and N. Torikai, *Nihon Reoroji Gakkaishi*, **36**, 113 (2008).
96. H. Watanabe, *Acta Polym.*, **48**, 215 (1997).
97. H. Watanabe, T. Sato, and K. Osaki, *Macromolecules*, **33**, 2545 (2000).
98. H. Watanabe and H. Tan, *Macromolecules*, **37**, 5118 (2004).
99. H. Watanabe, Y. Matsumiya, T. Sawada, and T. Iwamoto, *Macromolecules*, **40**, 6885 (2007).
100. H. Watanabe, Y. Matsumiya, J. Takada, H. Sasaki, Y. Matsushima, A. Kuriyama, T. Inoue, K. H. Ahn, W. Yu, and R. Krishnamoorti, *Macromolecules*, **40**, 5389 (2007).
101. J. Takada, H. Sasaki, Y. Matsushima, A. Kuriyama, Y. Matsumiya, H. Watanabe, K. H. Ahn, and W. Yu, *Nihon Reoroji Gakkaishi*, **36**, 35 (2008).
102. Q. Chen, Y. Matsumiya, Y. Masubuchi, H. Watanabe, and T. Inoue, *Macromolecules*, **41**, 8694 (2008).
103. Y. Hirose, O. Urakawa, and K. Adachi, *Macromolecules*, **36**, 3699 (2003).
104. O. Urakawa, *Nihon Reoroji Gakkaishi*, **32**, 265 (2004).
105. M. W. Matsen and M. Schick, *Macromolecules*, **27**, 187 (1994).
106. A. Takano, I. Kamaya, Y. Takahashi, and Y. Matsushita, *Macromolecules*, **38**, 9718 (2005).
107. Y. Takahashi, Y. H. Song, N. Nemoto, A. Takano, Y. Akazawa, and Y. Matsushita, *Macromolecules*, **38**, 9724 (2005).

Hiroshi Watanabe was born in 1957 in Takamatsu, Kagawa, Japan. He graduated from the Department of Macromolecular Science, Osaka University in 1979, and received his PhD from Osaka University in 1985. He joined the Department of Macromolecular Science, Osaka University as an assistant professor in 1983. He moved to the Institute for Chemical Research, Kyoto University as an associate professor in 1994 and promoted to a full professor in 2003 at Kyoto University. He received the Award of the Society of Polymer Science, Japan in 2008. His major research field is the dynamics and rheology of softmatters, and he is interested in slow dynamics in homopolymers, block copolymers, polymer blends, suspensions, and emulsions.